Title

Developmental constraints modulate reproductive fate and plasticity within the Arabidopsis ovule primordium

Elvira Hernandez-Lagana[1]*, Gabriella Mosca[2]*, Ethel Mendocilla Sato[2]*, Nuno Pires[2], Anja Frey[2,4], Alejandro Giraldo-Fonseca[2], Ueli Grossniklaus[2], Olivier Hamant[3], Christophe Godin[3], Arezki Boudaoud[3], Daniel Grimanelli[1], Daphné Autran[1#], Célia Baroux[2#]

Affiliations :

1 Diversité, Adaptation et Développement des Plantes (DIADE), IRD, CIRAD, University of Montpellier, Montpellier, France.

2 Department of Plant and Microbial Biology and Zurich-Basel Plant Science Center, University of Zürich, Zürich, Switzerland.

3 Laboratoire Reproduction et Développement des Plantes, University of Lyon, ENS Lyon, UCB Lyon 1, CNRS, INRAE, INRIA, Lyon, France.

4 Present address: Novartis Pharma Schweiz AG, Basel, Switzerland.

* equal contribution.

authors for correspondence: daphne.autran@ird.fr, cbaroux@botinst.uzh.ch

The authors declare no competing financial interests.

Running title

Developmental canalization and germinal fate in plant ovules

ORCID numbers

Name	Orcid #
Elvira Hernandez-Lagana	0000-0002-2645-3783
Gabriella Mosca	0000-0003-4509-498X
Ethel Mendocilla Sato	0000-0003-0339-3535
Alejandro Giraldo-Fonseca	0000-0003-2943-9810
Nuno Pires	0000-0002-7113-3519
Anja Frey	
Ueli Grossniklaus	0000-0002-0522-8974
Olivier Hamant	0000-0001-6906-6620
Arezki Boudaoud	0000-0002-2780-4717
Christophe Godin	0000-0002-1202-8460
Daniel Grimanelli	0000-0001-5424-114X
Daphné Autran	0000-0002-5227-8966
Célia Baroux	0000-0001-6307-2229

Summary

Sexual reproduction in multicellular organisms requires the separation of the germline from the soma. In flowering plants, the formation of spore mother cells (SMCs) marks the somatic-to-reproductive cell fate transition in floral organs. The female SMC differentiates at the apex of the ovule primordium, as a single, large, and elongated subepidermal cell. However, this singleness rule is not very robust: several SMC candidates develop in some *Arabidopsis* accessions and mutants. Yet, the basis of this plasticity is not understood. Here we investigate whether ovule primordium growth and overarching cellular architecture serve as an instructive cue to channel the formation of a single SMC. Combining quantitative analyses of 3D cell-based information, cell cycle reporters, and 2D growth simulations, we provide a comprehensive analysis of cell proliferation and growth events that shape ovule primordium development and SMC formation. This reveals that SMC characteristics emerge earlier than previously thought, and often for more than one cell. Thus, developmental constraints gradually canalize the fate of these cells, so that a single SMC enters meiosis ultimately. Among these constraints, we explore the contribution of dynamic cell division patterns and localized cell growth anisotropy. Consistent with 2D computational simulations, the reduction of anisotropy in *katanin* mutants leads to altered ovule shape and cell division patterns. Such disturbance of ovule morphology is sufficient to delay SMC canalization, as multiple cells express reproductive fate markers in *katanin* mutant ovules. In conclusion, we show that ovule growth and shape channel SMC fate for a single cell.

Keywords

ovule primordium, SMC, cell fate, canalization, *katanin*, growth, tissue mechanics, Arabidopsis

Highlights

1. SMC singleness emerges from a canalization process mediated by KATANIN.
2. Anisotropic cell growth and local, biphasic cell divisions patterns explain ovule primordium shape.
3. 2D-mechanical growth models relate ovule growth and SMC emergence.
4. A 3D image resource of developing ovule primordia at cellular resolution.

52 ## Introduction

53 A hallmark of sexual reproduction in multicellular organisms is the separation of the germline from the
54 soma. In animals, primordial germ cells (PGCs) are set-aside during embryogenesis from a mass of
55 pluripotent cells. The number of germ cells depends on the balance between proliferation (self-renewal)
56 and differentiation, a process controlled by both intrinsic factors and the surrounding somatic tissue [1,
57 2]. In flowering plants, by contrast, the spore mother cells (SMCs), representing the germline precursors,
58 differentiate late in development. SMCs arise multiple times, i.e., in each flower during the formation of
59 reproductive organs. In *Arabidopsis*, the female SMC differentiates in the nucellus of the ovule
60 primordium, a digit-shaped organ outgrowing from the placental tissue of the gynoecium. The SMC is
61 recognizable as a single, large, and elongated subepidermal cell, in central position, at the nucellus, and
62 displaying a prominent nucleus and nucleolus [3-6].

63 Although SMC singleness may appear to be robust, more than one SMC candidate *per* primordium can
64 develop at variable frequencies depending on the *Arabidopsis* accession (9,6% in *Columbia* (*Col-0*), 27%
65 in *Monterrosso* (*Mr-0)*, [7]). Mutants in *Arabidopsis*, maize, and rice that compromise SMC singleness
66 unveiled the role of regulatory pathways involving intercellular signaling, small RNAs, as well as DNA and
67 histone methylation [8-16]. As the SMC forms, cell-cycle regulation contributes to the stabilization of its
68 fate in a cell-autonomous manner through cyclin-dependent kinase (CDK) inhibitors and
69 RETINOBLASTOMA-RELATED1 (RBR1) [17, 18]. SMC singleness thus appears to result from a two-step
70 control: first, restricting differentiation to only one cell and second, preventing self-renewal before
71 meiosis (reviewed in [19, 20]).

72 However, the precise mechanisms underlying the plasticity in the number of SMC candidates and SMC
73 fate specification are still poorly understood. In principle, SMC singleness may be controlled by
74 successive molecular cues. However, even in that scenario, such cues must be positional, at least to
75 some extent, and thus involve a spatial component. In the last decade, many different molecular cues
76 defining spatial patterns in the ovule primordium were identified [16, 19], however their coordination is
77 unknown. Since SMCs emerge at the primordium apex concomitant with its elongation, we hypothesize
78 that developmental constraints during ovule morphogenesis influence SMC singleness and
79 differentiation. Such a scenario could explain variation in the number of SMC candidates, ultimately
80 culminating in a single SMC entering meiosis, a process that was previously discussed as a possible
81 canalization [7]. Canalization refers to the capacity of an organism to follow a given developmental

82 trajectory in spite of disturbances [21-23]. Yet, canalization as proposed by Waddington embraces a
83 broader meaning, including the nature of the developmental process itself to explain phenotypic
84 variability [21]. Answering the questions of whether SMC formation follows a stereotypical or plastic
85 developmental process and whether it is intrinsically linked to or independent of ovule primordium
86 growth would unravel fundamental principles connecting cell fate establishment and organ growth.
87 Such an analysis requires a high-resolution description of the ovule tissue topology and geometry in
88 time. Our current knowledge of ovule primordium growth in *Arabidopsis* is based on two-dimensional
89 (2D) micrographs from tissue sections or clearings. It is described in discrete developmental stages
90 capturing classes of primordia by their global shape and SMC appearance until meiosis and by the
91 presence of integument layers and ovule curvature later-on [24]. In addition, a 3D analysis of average
92 cell volumes during primordium growth was recently provided [25]. Yet, we lack a view of the patterning
93 processes shaping the early ovule primordium, the relation of cell layers and proliferation domains in
94 3D, and a temporally resolved description of primordium emergence. To address the question of SMC
95 singleness, we thus developed a resource where the growth of the ovule primordium is described and
96 quantified at cellular resolution in 3D. We combined 3D imaging, quantitative analysis of cell and tissue
97 characteristics, reporter gene analyses, 2D mechanical growth simulations, and genetic analyses. Using
98 the *katanin* mutant affecting anisotropic cell growth and cell division patterns [26, 27], we show that an
99 altered ovule morphology is sufficient to disrupt SMC singleness. We also uncovered that differentiation
100 of SMC candidates initiates earlier than previously thought. Finally, we provide evidence for a
101 developmental canalization process leading to the specification of a single SMC prior to meiosis.
102

Results

Building a reference collection of 3D images capturing developing ovule primordia in 3D at cellular resolution

To generate 3D reconstructions of ovule primordia with cellular resolution at consecutive different stages we imaged primordia stained for cell boundaries in intact carpels by confocal microscopy. Carpels were cleared and stained using a modified PS-PI staining [28] and mounting procedure preserving their integrity ([29],Figure 1A). We selected high signal-to-noise ratio images and segmented them based on cell boundary signals using a previously described pipeline ([29],Figure 1B). We manually curated 92 ovules representing seven consecutive developmental stages (7-21 ovules *per* stage, Figure 1B, Table 1, Data S1), classified according to an extended nomenclature explained in the STAR Methods. In order to gain temporal resolution, we defined new stages (stage 0-I to stage 0-III) covering primordium emergence, which occurs prior to the straight digit-shape organ stage 1-I where the SMC becomes distinguishable by its apparent larger size in longitudinal views [24].

To evaluate the distinct contribution of domain-, layer- and cell-specific growth dynamics, we assigned a label to each segmented cell enabling data classification (Figure 1B, STAR Methods). We defined cell labels to distinguish *domains*, *layers* and *cell types*: the apical and basal domains, the L1 and L2,L3 layers (L1, epidermis; and the underlying L2 and L3 layers taken together), and seven cell types intersecting with the domains and layers. The latter include the self-explanatory cell labels “L1 apical”, “L1 basal”, “L2,L3 apical”, “L2,L3 basal”, “SMC”, and specific labels for the “L1 dome”, the upmost apical L1 cells in contact with the SMC, and the “CC” or companion cells, the elongated L2 cells adjacent to the SMC.

To quantitatively analyze the data with respect to cell labels, layers, domains, ovule stage and genotype, we developed an interactive, R-based interface named OvuleViz. The script reads cell descriptors exported from segmented image files and enables multiple plot generation from a user-based selection of (sub)datasets (Figure S1A-C, STAR Methods). Collectively, our work generated a reference collection of annotated, 3D images capturing ovule primordium development at cellular resolution from emergence until the onset of meiosis. The collection of 92 segmented images associated with a total of 7763 annotated cells and five morphological cell descriptors (volume, area, sphericity, prolate and oblate ellipticity) provides a unique resource for morphodynamic analyses of ovule primordium growth.

135 To identify correlations between growth patterns and differentiation, we performed a principle
136 component analysis (PCA) based on the aforementioned cell descriptors, *per* cell type and stage,
137 considered together or separately (Figure S1D-E). In this global analysis, the SMC appears distinct at late
138 stages (2-I and 2-II) but clear conclusions are hampered by a crowding effect that is not resolved by this
139 approach. This prompted us to investigate in detail the contribution of different layers, domains, and
140 cell types to ovule primordium growth and in relation to SMC differentiation.
141

142 **Ovule primordium morphogenesis involves domain-specific cell proliferation and anisotropic cell**
143 **shape patterns**
144

145 The ovule primordium emerges from the placenta as a small dome-shaped protrusion and grows into a
146 digit-shaped primordium with nearly cylindrical symmetry (stage 1-I) before enlarging at the base
147 (Figure 1B). Using our segmented images, we first quantified global changes in cell number, cell volume,
148 and ovule primordium shape. Our analysis revealed two distinct phases of morphological events. Phase I
149 (stages 0-I to 0-III) is characterized by a 4.5-fold increase in total cell number but a moderate increase in
150 mean cell volume (10%, P=0.03). By contrast, Phase II (stages 1-I to 2-II) is characterized by a moderate
151 increase in cell number (50%) and the global mean cell volume is relatively constant (Figure 2A, S2A). To
152 quantify the resulting changes in organ shape, we extrapolated a continuous surface mesh of the ovule
153 outline and used it to compute its height and width at the base (Figure 2B-C, S2B, STAR Methods).
154 Anisotropic organ growth during Phase I was confirmed by a steady increase in height while primordium
155 width increased moderately (Figure 2C). This contrast in morphodynamic events between Phase I and II
156 is illustrated by the representation of fold-changes (FCs) in cell number and aspect ratio (Figure 2D)
157 which range between 1.5 and 2.0 in Phase I whereas drop to 1.4 and 1.2 in Phase II. These observations
158 confirmed that Phase I captures a distinct growth dynamic compared to Phase II.
159 Next, to capture possible specific patterns of growth, we analyzed cell number, cell size, and cell
160 shape using different viewpoints: one comparing the L1 and L2,L3 layers and one contrasting the apical
161 *vs* basal domains. Scoring cell number *per* viewpoint clearly showed a dominant contribution of the
162 epidermis (L1) relative to the subepidermal layers and of the basal relative to the apical domain (Figure
163 2E,F). To verify these findings with a cellular marker, we analyzed the M-phase-specific *CYCB1.1-dbGFP*
164 reporter [30]. We scored the number of GFP-expressing cells among 481 ovules and plotted relative
165 mitotic frequencies *per* cell layer and domain for each ovule stage to generate a cell-based mitotic
166 activity map (Figure 2G-H, Data S2, STAR Methods). In this approach, subepidermal cells beneath the

167 dome were distinguished from underlying L3 cells to gain resolution on the L2 apical domain where the
168 SMC differentiate. Consistent with our previous observation, in Phase I, a high proliferation activity was
169 scored in L1 cells at the primordium apex (scoring 64% of mitotic events). By contrast, the L2 apical
170 domain remains relatively quiescent (contributing only 3% of the mitotic events). During Phase II,
171 proliferation preferentially occurs in the basal domain with > 60% of mitotic events at all stages. It is
172 noteworthy that during this phase, L2 apical cells divide relatively rarely, with the exception of SMC
173 neighbors cells that show frequent divisions at stage 1-II. Thus, reporter analysis confirmed a biphasic,
174 temporal pattern of cell division with changing regional contributions, suggesting the L1 apical and L2,L3
175 basal domains as consecutive sites of increased proliferation, contributing to morphological changes in
176 Phase I and II, respectively.

177 Cell size analysis, by contrast, did not reveal significant changes during primordium development
178 with the notable exception of the SMC (Figure 2A, S2C). The SMC gradually attains a distinct size starting
179 at stage 0-III when compared to other L2,L3 cells (Figure 2I) or even earlier, at stage 0-I, when compared
180 to all other cells (Figure 2I inset). Size differentiation of the SMC is not uniform among ovules,
181 demonstrating plasticity in the process (Figure S2D). In addition, different cell sizes between L1 and
182 L2,L3 layers are already discernible at primordium emergence (Figure 2J, S2E). The presence of larger
183 L2,L3 cells is consistent with the low division frequency observed previously - likely stemming from
184 longer growth phases. We propose that cell size asymmetry established at early stages favors SMC
185 emergence.

186 We then investigated cell shape changes during primordium elongation, using ellipticity and
187 sphericity indices computed by Imaris (Bitplane, Switzerland) following segmentation. The analysis did
188 not reveal significant differences between domains or layers (Figure S2F, STAR Methods). This could
189 indicate either a highly variable cell shape or more localized, cell type-specific shape changes. We thus
190 more specifically analyzed the subepidermal niche where the SMC differentiates. We found that
191 companion cells showed an increasing ellipticity (and decreasing sphericity), starting at stage 1-I and
192 culminating at stage 2-I (Figure S2F). By contrast, the SMC only showed a moderate decrease in
193 sphericity at late stages and no distinctive ellipticity at early stages (Figure S2F). In order to get raw
194 information on anisotropy of cells shapes, we developed an extension for MorphoMechanX ([31],
195 www.morphomechanx.org) to (i) perform a semi-automatic labeling of cell layers and cell types from a
196 cellularized mesh and (ii) compute in each 3D cell the principal axes of shape anisotropy and the
197 corresponding indexes (Figure S2G, STAR Methods, Movie S1). The maximum anisotropy shape index of
198 the SMCs was, averaged *per* stage, consistently above the medium (and hence above the minimum)

199 anisotropy index (Figure 2K). This confirmed that the SMC has an anisotropic shape, with a
200 distinguishable major axis throughout ovule primordium development from early stages onwards
201 (Figure S2H). We measured the degree of alignment of the SMC major axis with the main growth axis of
202 the ovule during early stages (stage 0-II) and found a mean angle of 22° (+/- 11°, n=16) (Figure 2K, see
203 also Figure 2C showing main growth axis of the ovule along development). Thus, the SMC's anisotropic
204 shape emerges at the earliest stages and its orientation is aligned with the growth axis of the
205 primordium.

206 Taken together, these results suggest that anisotropic primordium growth is linked to domain-
207 specific cell proliferation combined with localized, anisotropic expansion.

208

209 2D mechanical simulations of ovule primordium development relate its coordinated growth to SMC 210 shape emergence

211 Organ shape is determined by the rate and direction of cell growth, the latter affected by signaling and
212 the mechanical state of the tissue and its geometry, with possible feedback interactions between them
213 [32, 33]. Mechanical constraints arise from the growth process in form of tensile and compressive forces
214 that, in turn, influence cell and tissue growth depending on their elastic/visco-plastic properties [33]. To
215 determine the role of ovule primordium growth on SMC differentiation, which involves early differential
216 cell growth, we sought to understand the contributions of growth rate and anisotropy and their relation
217 to signaling and mechanical constraints [34, 35]. Resolving this question would define fundamental
218 developmental principles linking organ growth and SMC differentiation.

219 We first sought to determine morphogenetic principles of primordium growth at the tissue level by
220 developing a 2D Finite Element Method (FEM)-based mechanical model, which considered two
221 uncoupled but complementary modes of growth: (i) signal-based growth in which an abstract
222 morphogen captures the cumulative effects of biochemical signals without considering its explicit mode
223 of action (i.e., cell wall loosening, increase in turgor pressure) [36]; and (ii) passive strain-based growth
224 in which relaxation accommodates excess of strain (and therefore also excess of stress) that
225 accumulated in the tissue by relaxing its reference configuration according to the amount of strain. The
226 mechanical equilibrium is computed to ensure compatibility with the tissue that is locally growing at
227 different rates and orientations. This introduces residual internal compressions and tensions to which
228 the action of turgor pressure is also added [37]. A polarization field is used to set the direction of
229 anisotropic growth for both growth mechanisms [34]. The simulation consists of iterations where the

230 mechanical equilibrium is computed before each growth step is specified by signal- and strain-based
231 growth. This strategy extends previous tissue growth models ([36, 38-40], STAR Methods).
232 We designed a starting template consisting of an L1 layer distinct from the underlying L2, L3
233 tissue based on different growth and material properties (Table 2, Figure S3, STAR Methods). We first
234 set the model components to produce a realistic elongated, digit-shaped primordium with a narrow
235 dome and an L1 layer of stable thickness during development (Reference Model, FEM-Model 1) (Figure
236 3A, S3A). This model combines the following hypotheses: a narrow domain of anisotropic, signal-based
237 growth, a broad domain competent for passive strain-based relaxation and material anisotropy.
238 Then, using the versatility of the modeling framework to vary initial conditions, we asked
239 whether primordium morphogenesis is driven primarily by growth of the epidermis (L1) or if it requires
240 active growth of inner tissues. In the first scenario, L1 growth is responsible for creating a dome shape,
241 enabling underlying tissue growth by pulling on the inner layers and inducing cell divisions as observed
242 in Phase I. In another scenario, active growth of the inner tissues forces the L1 to grow and create a
243 protrusion. We ran several simulations with varying initial distribution patterns of the growth signal
244 (Table 2). The shape aberrations produced by FEM-Models 4, 5, 6 and 7 (Figure S3B) suggested that an
245 inner tissue-driven growth principle (*vs* L1-driven), involving a narrow strip of initial growth signal
246 diffusing in the inner layers, was more plausible (Reference Model, FEM-Model 1, Figure 3A, S3A). Next,
247 through modulation of passive strain-based growth, we determined that a broad tissue domain
248 uniformly competent for strain accommodation is necessary to resolve the high accumulation of strain,
249 limiting primordium elongation (FEM-Model 8, Figure S3C). Yet, material anisotropy influencing the
250 relaxation response is not necessarily required broadly and it is sufficient to specify it in the L1 only to
251 achieve a dome with a realistic shape and constant L1 thickness (FEM-Model 2, Figure S3C). Finally, we
252 asked whether growth anisotropy must be specified in the model or if geometrical and mechanical
253 constraints are sufficient to specify primordium shape. Clearly, removing this component abolished the
254 digit shape of the primordium and produced a hemi-spherical protrusion (FEM-Model 3, Figure 3B).
255 In summary, we identified parsimonious growth principles shaping the ovule primordium: an
256 inner tissue-driven process promoted by a narrow domain of anisotropic, signal-based growth is
257 complemented by passive tissue growth in response to accumulated strain. Furthermore, material
258 anisotropy in the L1 is predicted to play a role in constraining L1 thickness as observed experimentally.
259 Next, we aimed to analyze how cell division and cell shape, particularly that of the SMC, are
260 connected to tissue growth patterns at cellular scale. For this, we developed a complementary model
261 with cellular resolution. This vertex-based model features cells as 2D polygons whose walls are mass

262 spring (MS) segments [41, 42]. This model integrates mechanics (Hooke's law for MSs) with signal- and
263 strain-based growth as before (STAR Methods). We simulated growth starting with a virtual grid of cells
264 representing a flat placenta and focused on early stages of ovule primordium formation until stage 1-I.
265 We tested the same combination of growth hypotheses as for the continuous model (Table 2), except
266 for material anisotropy that cannot easily be embedded in a vertex-based model. As we observed that
267 L1 cells do not divide periclinally, nor change in volume on average, we deduced that their growth
268 occurs mainly in direction of the main axis of the primordium. For this reason, we enforced this feature
269 in our model, preventing growth of the anticlinal walls (both for signal-based growth and passive strain-
270 based growth, STAR Methods). This constraint limits the ways an organ can grow in a digit-shaped
271 fashion, as the L1 does not progressively populate the inner tissues by division. Furthermore, our models
272 included assumes a slower division rate for L2,L3 apical cells, consistent with our previous observations
273 (Figure S3D).

274 We identified MS-Model 2 to best capture the characteristic shape and aspect ratio of ovules
275 (Figure 3C, S3D). This reference model confirmed the growth hypotheses from FEM-based simulations
276 regarding the distribution and orientation of signal-based growth (Figure S3B) and passive strain-based
277 growth (Figure S3C).

278 Finally, we were interested to determine whether SMC morphology is an emerging property of
279 primordium growth and how anisotropic growth influences the process. Remarkably, in the cell-based
280 reference model including anisotropic cell growth, an SMC candidate emerged early: a central L2 apical
281 cell that, beside its larger size, adopted a trapezoidal shape and a principal anisotropy axis aligned with
282 the main direction of ovule growth (Figure 3E). Such features are qualitatively comparable what we
283 observed for stage 0-II primordia (Figure 3E, S3D, Figure 2K).

284 The MS-Model 3 corresponds to a virtual mutant with isotropic cell growth. Under these
285 conditions, ovule primordia displayed an altered shape with a wider surface and flatter dome as in the
286 FEM-Model 3 (Figure 3D). Interestingly, a larger, central L2 cell still emerged but the elongated shape
287 typical of SMCs arose later in the simulation progression as compared to the reference model (Figure 3F,
288 Movie S3). Thus, 2D simulations predict that anisotropic cell growth does not only affect ovule
289 primordium shape but also the timing of SMC candidate emergence, hence connecting the growth
290 process with SMC differentiation. In these models, the candidate SMC eventually divided as they missed
291 a causative rule to differentially regulate cell division. When we prevented the SMC candidate to divide,
292 its enlargement overrode primordium shape control in our simulations, indicating an additional level of
293 control in real primordia (Figure S3E).

294 Altogether, the two complementary growth models of ovule primordium development confirm
295 at different scales a role for regional cell growth compatible with previous observations. They predict
296 that tissue accommodation, anisotropy in mechanical properties, and a specific pattern of signal-based
297 growth collectively influence the directional growth of the primordium. We showed that altered ovule
298 primordium growth affects size and shape of the SMC candidate, linking organ architecture to SMC fate.
299 Reciprocally, unleashing SMC growth leads to deformation of the primordium, suggesting the existence
300 of a compensatory feedback mechanism that coordinates cell and organ growth.
301

302 ### *katanin* mutants show a distinct ovule primordium architecture primarily through altered cell division
303 patterns

304
305 To test the model predictions experimentally, we analyzed the consequences of cell growth anisotropy
306 perturbation on ovule primordium growth and SMC fate establishment. *Arabidopsis* plants carrying a
307 defective microtubule-severing protein KATANIN exhibit organ shape defects, including increased round-
308 and bumpiness, as a consequence of disorganized cortical microtubules and isotropic cellulose
309 microfibril orientations [43, 44]. We thus analyzed the shape and cellular organization of ovule
310 primordia in *katanin* mutants using the *botero* (*bot1-7*) (*Ws* background), *lue1*, and *mad5* alleles (*Col*
311 background) [43, 45, 46], collectively referred to *katanin* - noted *kat*- mutants hereafter. We generated
312 and analyzed a new dataset of 59 annotated 3D digital *kat* and corresponding wild-type ovule primordia
313 at stages 0-III, 1-I, and 1-II (Data S4a). *kat* mutant primordia have an increased size and a more isotropic
314 shape (Figure 4A), being 1.5 times bigger in volume than wild-type primordia (P=0.007, stage 0-III, Figure
315 4B) with a smaller aspect ratio (P<0.01 stages 1-I, 1-II, Figure 4C). The width-to-height aspect ratio does
316 not inform on the shape at the flanks, hence does not discriminate straight digit *versus* plump organ
317 shapes. We estimated the "plumpiness" of the primordia by calculating the volume fraction of a fitting,
318 3D parallelepiped (bounding box) effectively occupied by the primordium (bounding box occupancy,
319 Figure 4D, S4A). In *kat* ovules, the relationship deviates from the wild type beginning at stage 1-I, when
320 the primodium normally starts elongating along the major growth axis. These measurements confirmed
321 a marked attenuation of anisotropic growth in *kat* ovule primordia as was observed in roots, shoot
322 organs, or seeds [43, 47-52]. Yet, at a global level, the mean cell number, cell volume, and sphericity are
323 not significantly different between *kat* and wild-type primordia (Figure S4B-C). Thus, these global
324 approaches did not resolve the origin of primordia mis-shaping.
325 To refine the analysis, we contrasted different layers as done for wild-type primordia and found
326 local alterations that provide an explanation for the formation of broader and more isotropic primordia

327 in *kat* mutants. Notably, the epidermis of *kat* primordia contains 17.5% more cells (47 L1 cells in *kat* vs
328 40 in wild-type at stage 0-III, P=0.03). Also, *kat* epidermal cells have a 20% larger volume than in the wild
329 type (P<0.001). Early in development (stage 0-III), the apical domain of *kat* primordia is populated by
330 larger (17%, P<0.001) and more spherical (2%, P<0.001) cells, than in wild type (Figure 4E,S4D), a
331 characteristic that extends to the basal domain at later stages (Figure S4D). To determine whether, in
332 *kat* primordia, the mitotic domains shifted in space and/or time, we scored *CYCB1.1-dbGFP* signals *per*
333 stage, layers, and equivalent domains as before, and expressed it as fold-changes relative to wild-type
334 primordia (Figure 4F, S4E). In Phase I (stage 0-II), we consistently scored 2.4 times less mitoses in the L1
335 dome domain, and 2.7 times more mitoses at the L1 basal domain of *kat* primordia. Hence, in *kat*
336 primordia, proliferation is mostly localized in the basal region and not higher in the early L1 dome as in
337 the wild type.

338 To elucidate whether these alterations affected the cellular domain where the SMC normally
339 differentiates, we interrogated L2 apical cells and specifically the L2 neighbors of the candidate SMC. At
340 stage 0-II, we scored 3.5 times more divisions in the L2 SMC neighbor cells in the apical domain, showing
341 that the relative mitotic quiescence is lost in this domain in *kat* primordia. Next, we focus on cells in
342 contact with the SMC (STAR methods). We found that in *kat* primordia, in contrast to the wild type and
343 to non-neighbor cells, SMC neighbors specifically enlarge as early as stage 0-III (Figure 4G, S4E) but
344 without a detectable increase in sphericity. Consistently, our *CYCB1.1-dbGFP* analysis showed that the
345 mitotic activity detected in SMC neighbors at stage 1-II in wild-type primordia significantly decreases in
346 *ka*t primordia (Figure 4F, S4E).

347 In conclusion, the absence of *KAT*-mediated cell growth anisotropy is associated with major
348 changes in the domains of cell division, which can be linked to geometric changes or to a slow-down of
349 mitosis as previously shown in *kat* mutants [27, 53]. These alterations impact the shape of the ovule
350 primordium, but also the architecture of the subepidermal apical domain, where the SMC differentiates.
351

352 **Altered ovule primordium architecture in *katanin* mutants induces ectopic SMC fate**
353

354 We next investigated whether *kat* ovule growth defects also affect cell identity and SMC singleness. In
355 *kat* primordia, SMCs appear bigger in volume and more spherical than their wild-type counterparts at
356 stage 0-III; yet, no significant differences were detected at stages 1-I and 1-II. However, we observed
357 variability in volume at these stages (Figure 4G, 5A, S5A). When we analyzed the number of SMC
358 neighbors (Figure 5A-B), we found seven or more in *kat* primordia compared to an average of five in the

359 wild type. The *kat* SMC neighbors were 14% larger (P=0.006), 11% less ellipsoid (P=0.03), and 2% more
360 spherical (P<0.01) than in the wild type (Figure 5B), reminiscent of mutants affecting SMC singleness
361 [19].

362 To analyze the identity of these additional, enlarged cells, we quantified several SMC hallmarks.
363 First, we found that ~ 35% *kat* primordia harbor more than one SMC candidate at stage 1-II, decreasing
364 to 14.42% at stage 2-II (Figure 5C). Then, we assessed two complementary markers associated with SMC
365 fate in *kat* primordia. The first marker is a GFP-tagged linker histone variant (H1.1-GFP) that marks the
366 somatic-to-reproductive fate transition by its eviction in the SMC at stage 1-I [54]. H1.1-GFP eviction
367 occurred in more than one cell in 28.57% *kat* primordia (n=43, Figure 5D). The second marker reports
368 expression of the *KNUCKLES* transcription factor (KNU-YFP) expressed in the SMC [55]. Detectable as
369 early as stage 1-I in the wild type, it was ectopically expressed in 21% *kat* primordia at stage 1-II (n=43)
370 (Figure 5E, S5B). To test whether the ectopic SMC candidates have a meiotic competence, we analyzed
371 the AtDMC1-GUS reporter [56, 57], and indeed scored ectopic expression in 57% of *kat* primordia (n=56)
372 (Figure 5F). We also analyzed the pWOX2-CenH3-GFP marker labeling centromeres starting at the
373 functional megaspore stage [58] and found 20.7% *kat* primordia (n=29) with two labeled cells, as
374 compared to 3,8% (n=26) in the wild type (Figure S5C).

375 Taken together, these results show that ectopic, abnormally enlarged SMC neighbors in *kat*
376 primordia show at least some characteristics of SMC and/or functional megaspores and can thus adopt a
377 reproductive fate.

378

379 **The growth of a single SMC emerges from a canalization process**

380 Based on our analysis of *kat* primordia, it appeared that the frequency of ectopic SMC candidates was
381 high at early stages but decreased over time (Figure 5C). This is reminiscent of the phenotypic plasticity
382 in SMC differentiation observed, to a lesser degree, in different *Arabidopsis* accessions [7]. To
383 characterize this plasticity during development we analyzed 1276 wild-type primordia from stage 0-II to
384 2-II and scored the number of primordia with one or two enlarged, centrally positioned, subepidermal
385 cells (class A and B, respectively, Figure 6A-C). In the wild type, the majority of primordia showed a
386 single candidate SMC (class A) at the stage 0-II, but 27% primordia (n=289) had two SMC candidates
387 (class B), this frequency decreasing to 3% at stage 2-II (n=103). This finding is consistent with ~ 5%
388 primordia in wild-type at stage 1-II showing H1.1-GFP eviction (n=43) and KNU-YFP expression (n=88) in
389 more than one cell, respectively (Figure 5D-E).

390 Next, we quantified class A and B primordia in *kat* mutants by scoring 2587 ovules of three
391 alleles (Figure 6C, S6A). Clearly, the canalization process is delayed in *kat* mutant primordia with 33%
392 class B primordia at stage 1-II (n=113) compared to 12% in the wild type (n=281). Consistently, the two
393 previously used SMC markers are observed in ectopic cells in *kat* primordia already at stage 1-I (Figure
394 S6B-C), and more significantly at stage 1-II (28.5% ectopic eviction of H1.1-GFP and 21% ectopic
395 expression of KNU-YFP, Figure 5D-E). At stage 2-II, when 17% of cleared *kat* primordia (n=110) showed
396 ectopic SMCs, H1.1-GFP eviction and KNU-YFP expression was only found in 8% (n=25) and 6.7% (n=74)
397 of the primordia, respectively (Figure S5B-C). Therefore, developmental canalization is not only delayed
398 in *kat* ovules, but there is also a partial uncoupling of cellular morphology and marker expression.
399 Another outcome of this study is the early emergence of SMCs, confirming our former 3D cell-
400 based analysis that showed heterogeneity in cell volume of the L2,L3 apical cells already at stages 0-I/0-
401 II (Figure 2J). To corroborate this finding using a different criterion, we measured the nuclear area,
402 which is a distinctive feature of SMCs [7, 54]. We compared the nuclear area of SMC candidate to that of
403 surrounding L1 and L2 cells in both class A and B primordia at stages 0-II and 0-III. Wild-type class A and
404 B primordia showed an enlarged nucleus in the candidate SMCs from stage 0-II onwards. This correlation
405 was also true in *kat* primordia, where SMC candidates also showed a 1.37-fold increase in nuclear size
406 compared to the wild type (Figure 6D, S6D-E).
407 The commitment to SMC fate is difficult to resolve at early stages due to the lack of molecular
408 markers. Building on our previous findings, we rationalized that cells from the L2 apical domain with a
409 low frequency of mitotic events could have started to transit toward S-phase. To learn more about cell
410 cycle progress in this domain, we analyzed a GFP-tagged PCNA variant marking the replication
411 machinery [59]. When engaged at active replication forks, PCNA-GFP shows nuclear speckles
412 characteristic of S-phase [60]. By contrast, it remains in the nucleoplasm in G1- and G2-phase and is
413 undetectable in M-phase. We quantified the nuclear distribution patterns of PCNA-GFP in cells from the
414 L2 apical domain in wild type and *kat* primordia separately for class A and B ovules (Figure 6E-H). At
415 stages 0-II and 0-III, PCNA-GFP was always detectable in both classes, indicating that L2 apical cells are
416 rarely in M-phase, consistent with the *CYCB1.1-dbGFP* marker analysis. Although the majority of class A
417 and B ovules at these stages showed a nucleoplasmic pattern, a significant proportion exhibited the
418 speckled S-phase pattern (Figure 6F). At stage 0-II, 24% of class A ovules (n=112) showed the S-phase
419 pattern in a single, centrally positioned apical cell (candidate SMC), reaching nearly 40% at stage 0-III
420 (n=79) (Figure 6F). Conversely, SMC neighbors rarely showed the S-phase pattern (2 to 5%). In class B
421 ovules, 30% (n=41) and 28% (n=60) at stages 0-II and 0-III, respectively, exhibited the S-phase pattern in

422 at least one of the cells in the apical domain (Figure 6F). Together with our analysis of the *CYCB1.1-*
423 *dbGFP* marker, these data suggest a prolonged S-phase in SMC candidates in Phase I (stages 0-II, 0-III).
424 Although it is not possible to resolve mitotic *versus* meiotic S-phase, it is tempting to speculate that this
425 is typical for the latter.

426 At the onset of Phase II, PCNA-GFP showed a nucleoplasmic pattern in the SMC of class A ovules
427 and in the L2 apical cells of class B ovules (Figure 6G-H, S6G-H). This is consistent with the detection of
428 newly replicated DNA in the SMC at stage 1-I [54]. In contrast to the SMC, the SMC neighbors display the
429 S-phase pattern (Figure 6G-H), consistent with the late divisions reported for these cells in Phase II
430 (Figure 2D). In *kat* primordia, we found an higher frequency of S-phase patterns in SMC candidates in
431 both class A and B ovules in Phase II (Figure 6H, S6F,H) and a lower frequency for SMC neighbors in class
432 A ovules at stages 1-I and 1-II, consistent with the deregulation of *CYCB1.1-dbGFP* in these cells in *kat*
433 primordia.

434 Collectively, our data indicate a cellular heterogeneity in the L2 apical domain that leads to the
435 emergence of one or several SMC candidates as early as stage 0-II. The gradual decrease in the number
436 of primordia with ambiguous SMC candidates suggests developmental canalization associated with a
437 cell-cycle progression, cellular elongation, and robust expression of SMC fate markers. In *kat* primordia
438 displaying architecture alterations, SMC singleness is largely disrupted: the selection of a single SMC is
439 significantly delayed and several SMC candidates persist in an ambiguous cell fate state.
440

441 **Discussion**
442

443 Organogenesis involves coordinated cell division and cell expansion, complex growth processes
444 orchestrated by biochemical and mechanical cues [33]. How cell differentiation is coordinated in space
445 and time during organ growth and whether these processes are interrelated are core questions for the
446 elucidation of patterning principles [61].

447 Here, we tested the hypothesis that ovule primordium growth and overarching organ
448 architecture determines the differentiation of a single SMC, the precursor cell of the female germline,
449 *per* primordium. We established a reference collection of images capturing ovule primordia in 3D at
450 cellular resolution to study how SMC cell fate relates to organogenesis in space and time. This reference
451 set populates a growing number of 3D-segmented images of plant tissues and organs, produced as
452 described here or with new tools for automated analyses [62]. This is a pre-requisite to generate a

453 developmental atlas that will integrate organ morphology at cellular resolution and gene expression
454 [63].

455 We report on an exhaustive morphodynamic analysis at cellular resolution, *per* stage, domain,
456 layer, and cell type of the ovule primordium. In combination with reporter gene analyses in wild-type
457 and mutant ovules and tissue growth simulations, this approach aims to elucidate fundamental
458 patterning principles. We found that cell division is not uniformly distributed in space and time and
459 follows a biphasic pattern where proliferation frequencies in L1 and L2,L3 domains alternate between
460 Phases I and II to shape the primordium. Strikingly, the L2 apical domain shows a low mitotic activity in
461 Phase I (stages 0-II, 0-III) with a prolonged S-phase in the SMC candidate. This is reminiscent of the
462 animal germline, where mitotic quiescence is a prerequisite to initiate meiosis [2, 64] and suggests a
463 functional analogy between the L2,L3 apical domain in ovule primordia and the primordial germline
464 niche in animals. Subsequently, the onset of Phase II coincides with the marked elongation and mitotic
465 quiescence of the SMC, contrasting with active divisions in the basal domain. Thus, the fate of the SMC
466 may be uncoupled early from that of the surrounding cells.

467 Tissue growth simulations allowed us to test the role of three main factors contributing to ovule
468 primordium patterning: i) anisotropic cell growth, ii) spatially confined specified growth signal along the
469 ovule axis, and iii) passive strain–based growth (*i.e.* the baseline competency of the tissue to
470 accommodate to accumulated strain, independently of growth signal). Omitting any of these factors, the
471 resulting models failed to shape a realistic primordium. In particular, isotropic growth produces
472 hemispheric instead of digit-shaped primordia with a flat dome resembling *kat* primordia, in which
473 anisotropic cell growth is altered [26]. Thus, the *kat* mutant phenotype provides an *in planta*
474 confirmation of our theoretical models. Furthermore, the observation that abnormally shaped *kat*
475 primordia contain cells with ectopic expression of SMC fate markers is consistent with the hypothesis
476 that organ growth and ovule primordium architecture control SMC differentiation.

477 Moreover, our results highlight the developmental constraints for differentiation of a single SMC
478 corresponding to a canalization process. The formation of a single SMC prevails in most angiosperms
479 [65]. Yet, some *Arabidopsis* accessions develop ovule primordia with multiple SMC candidates but
480 ultimately only one SMC is committed to meiosis [7, 24]. Our quantifications in two reference accessions
481 (Col-0, Ws) suggest that natural variation affects the timing of the canalization process. Canalization,
482 referring to a progressive constraint of cell fate choice, is well studied in animal systems where it is
483 modulated by intercellular signal-based feedback mechanisms [66] and epigenetic regulation [67].
484 Possibly, the epigenetic and signal-based processes known to regulate SMC differentiation also operate

485 in SMC fate canalization. In addition, the contribution of morphogenetic processes on cell fate
486 specification was recently re-evaluated in the light of tissue mechanics and patterning processes [68].
487 Our results are consistent with a role of primordium growth constraints on SMC fate canalization.
488 Possibly, the prolonged cell cycle of subepidermal cells in Phase I leverages competitive cell growth on
489 which canalization can operate. Under this scenario, disturbance of growth homeostasis as in *kat*
490 mutants would render this process ineffective and lead to a higher frequency of primordia with
491 unresolved SMC candidates, unveiling a coupling of SMC fate canalization with organ growth (Figure 6I).
492 De-canalization observed in *kat* mutants is consistent with recent work in *Drosophila* embryos showing
493 that organ shape contributes to developmental canalization [69]. Interestingly, the formation of a
494 broader dome in *kat* ovule coincides with the formation of a broader inner domain with more cells with
495 an unresolved SMC fate. This is reminiscent of the shoot apical meristem where the shape of the dome
496 correlates with the size and position of domains expressing stem cell regulators, such as WUSCHEL and
497 CLAVATA3 [70].

498 Epidermal growth controls shoot apical meristem and shoot growth through the modulation of
499 the expression domains of key regulators in the underlying layers [70, 71]. Whether growth of the
500 epidermis similarly controls the cell cycle and SMC fate regulators in underlying layers of ovule
501 primordia is an exciting question for future investigation, particularly considering the role of mechanical
502 constraints on gene regulation [72, 73]. Reciprocally, the role of the underlying layers for epidermis
503 growth and dome shape remains to be determined. Our ovule growth simulations predicted a role for
504 inner tissue-driven growth, similar to what has been proposed for the emergence of leaf primordia [74],
505 although this remains debated [36]. Moreover, our simulations suggested that passive strain-based
506 growth in the L1 is necessary to achieve a normal primordium shape, and that anisotropic material
507 properties in this layer are required to constrain the relaxation along the main axis of the primordium. A
508 possible explanation for this is the requirement to resolve mechanical conflicts arising between tissue
509 layers that grow at different rates [75]. This would be consistent with the high proliferation activity in
510 the L1 dome at a stage of marked differential growth of the SMC. In this scenario, divisions in L1 may
511 release the mechanical stress generated by SMC growth, leading to anisotropic organ growth.
512 Consistent with this idea, we observed that reduced organ shape anisotropy in *kat* ovules is associated
513 with fewer divisions in the L1 dome. The higher division rate in the wild type might confer higher
514 flexibility for the L1 to bend and follow an anisotropic growth profile driven by the inner layers. By
515 contrast, in *katanin*, non-dividing and elongated cells in the L1 would be expected to transmit higher

516 tension preventing bending. Experimental alterations of properties in L1 or L2,L3 cells, together with 3D
517 modeling, would be required to explore such scenarios.
518 Cell-based models suggested that blocking divisions in the SMC enables it to grow and push on
519 the surrounding cells, affecting significantly the ovule morphology. Therefore, we speculate that, in
520 order to maintain ovule growth homeostasis, differential SMC growth must adapt to the constraints
521 provided by surrounding cells. A gradual reduction of SMC turgor pressure may provide a plausible
522 cause to limit SMC size and maintain correct ovule anisotropy. Due to the limitations of 2D MS-based
523 models, such predictions will need to be tested in 3D cell-based models able to properly reproduce a
524 mechanical scenario for a growing ovule primordium. Nonetheless, this prediction paves the way to
525 further investigate the potential role of turgor pressure gradients across a field of cells, which could
526 provide positional information through the directional movement of water and other molecules,
527 thereby linking organ growth homeostasis, cell growth, and cell fate [76, 77]. Such mechanisms could
528 participate in defining the specific pattern of a growth signal predicted by our simulations. However, the
529 nature of the growth signal(s) and the mechanism(s) establishing its pattern in the placenta prior to
530 primordium emergence remain to be identified. Candidate signals may be the many differentially
531 localized hormones, gene products, and small RNAs known to affect ovule primordium growth [16, 19].
532 For example, in Phase II, auxin responses are restricted to the L1 dome while cytokinin signaling is
533 confined to a region basal to the SMC [78]. Whether this pattern is established already in Phase I and
534 plays a causative role in primordium patterning and SMC differentiation remains to be determined.
535
536

537 ## Author contributions

538 CB, DA, GM, EHL, DG, OH, AB, CG: Conceptualization; EHL, GM, CB, DA, OH, AB, CG, DG: Methodology;
539 GM, NP, AG: Softwares; EHL, GM, EMS, DA, CB: Validation; EHL, GM, AG, DA, CB: Formal analysis; EHL,
540 EMS, DA, CB: Investigation; EMS, AF, OH: Ressources; EHL, GM, NP, DA, CB: Data curation; EHL, GM,
541 EMS, DG, DA, CB: Writing – Original Draft; EHL, GM, OH, AB, CG, UG, DG, DA, CB: Writing – Reviewing
542 and Editing; EHL, GM, DA, CB: Visualization; CB, DA, DG, OH, AB, UG: Supervision; CB, DA, DG: Project
543 administration; CB, DA, DG, OH, AB, CG, UG: Funding Acquisition. All authors reviewed and revised the
544 manuscript.

545 ## Data availability

546

547 All materials, scripts and datasets generated and analyzed in the current study are available at
548 repositories (see Star Methods) or from the corresponding authors upon reasonable request.

549 ## Acknowledgments

550

551 We thank S. Strauss (Max Planck Institute for Plant Breeding Research, Cologne, Germany) and B. Lane
552 (John Innes Centre, Norwich, U.K.) for providing code and assessment for mesh generation and
553 simulations; S. Guyer (Bitplane, Switzerland) and M. Lartaud (CIRAD, France) for their help with IMARIS
554 analyses; O. Leblanc (IRD Montpellier, France) for his help with data visualization in R; the Montpellier
555 imaging facility MRI, member of the national infrastructure France-BioImaging supported by the French
556 National Research Agency (ANR-10-INBS-04) and the Center for Microscopy and Image Analysis of the
557 University of Zurich (ZMB) for microscopy imaging infrastructures; M. Ueda (Nagoya University, Japan),
558 I. Siddiqi (Center for Cellular and Molecular Biology, India), N. de Storme (Katholieke Universiteit Leuven,
559 Belgium), S. Matsunaga (Tokyo Science University, Japan), M. Tucker (University of Adelaide, Australia),
560 and the NASC stock center for seed germplasms.

561 This work was funded by the University of Zurich, IRD, and a PRCI grant from the Agence Nationale de la
562 Recherche/Swiss National Science Foundation (n°ANR-16-CE93-0002-01 to 04) to CB and DA; a grant
563 from the Swiss National Science Foundation (n° 310030B_160336) to UG, a CONACYT fellowship
564 (n°438277) to EHL, and a fellowship from the Forschungskredit of the University of Zurich (n°FK-74502-
565 04-01) to GM.

566

567 ## Figures legends
568
569 **Figure 1. Reference set of 3D segmented images capturing Arabidopsis ovule primordium growth at**
570 **cellular-resolution.**

571 (A) 3D reconstruction of a whole gynoecium stained with PS-PI (cell wall dye) and visualized by
572 CSLM. The cross section allows showing the nascent ovule primordia attached to the placenta.
573 (B) Ovule primordium developmental stages (0-I to 2-II) and organ viewpoints (domains) defined for the
574 3D quantitative analysis. All segmented data can be analyzed by an interactive interface named
575 OvuleViz. See also Figure S1A-C.
576 n= number of ovules analyzed. Segmented images for all developmental stages are provided in Data S1. See
577 also Figure S1 D-E, STAR Methods.
578
579 **Table 1. Classification criteria of Arabidopsis ovule primordia.**

580 The table summarizes general characteristics of ovule primordia per stage: cell "layers" above the
581 placenta scored as the number of L1 cells in a cell file drawn from the basis to the top, range thereof,
582 total cell number, ovule shape including height, width, aspect ratio.

583

584 **Figure 2. Ovule primordium morphogenesis involves domain-specific cell division and anisotropic cell**
585 **growth patterns.**

586 (A) Mean cell number *per* ovule increases mainly during stages 0-I to 0-III (Phase I), whereas cell volume
587 *per* ovule remains constant on average across primordium development (stages 0-I to 2-II).
588 (B) Representative image of a continuous surface of an ovule primordium mesh and its projected
589 median plane. Dashed lines indicate the minimal and maximal curvature points used to measure organ
590 height and width. Color scale: minimal curvature mm-1 (see also Figure S2B).
591 (C) Anisotropic organ growth during Phase I and until stage 1-II. Mean width and height were quantified
592 *per* stage.
593 (D) Phase I captures a distinct growth dynamic compared to Phase II. Fold-change of cell number and
594 aspect ratio between stages are plotted.
595 (E) Mean cell number is increased at the L1 *versus* L2,L3 layers across developmental stages.
596 (F) Mean cell number is increased in the basal *versus* apical domain across developmental stages.
597 (G) Representative images of ovule primordia expressing the M-phase reporter *pCYCB1.1::db-GFP.*
598 White arrows indicate dividing cells. Magenta signal: Renaissance SR2200 cell-wall label. Scale bar:
599 10µm.
600 (H) Domain-specific map of mitotic activity during ovule primordium development, scored using the
601 *pCYCB1.1::db-GFP* reporter. The frequency of mitoses was calculated *per* ovule domain at each
602 developmental stage and color-coded as indicated in the bar (right). n: total number of scored ovules.
603 (I) Mean SMC volume (dark blue) is significantly increased as compared to L2,L3 cells (pale blue) from
604 stage 0-III onward, on even at earlier stages as compared to all other cells (inset).

605 (J) Mean cell volume is increased in L2,L3 cells as compared to L1 cells, at the two early developmental
606 stages (st0-I, st0-II).
607 (K) The SMC consistently displays anisotropic shape with main axis of elongation aligned with ovule
608 growth axis. The SMC anisotropy index (boxplot, left; stage 0-II, n=16 ovules) was calculated from the
609 Maximum (dark blue), Minimum (light blue) and Medium (medium blue) covariance matrix eigenvalues,
610 computed from 3D segmented cells (see Figure S2G). Image (middle): illustration of the SMC main
611 anisotropy axis (orange arrow) related by an angle 'alpha' to the main axis of the ovule primordium
612 (white arrow), stage 0-II. Radar plot (right): 'alpha' angle measured on z projections for n=16 ovule
613 primordia at stage 0-II. See also Star Methods.
614 Error bars: Standard errors to the mean. Differences between cell types or primordium domains were
615 assessed using a two-tailed Man Whitney U test in (A) and (I); a two-tailed Wilcoxon signed rank test in
616 (J). *p≤0.05, **p≤0.01, ***p≤0.001. See also Figure S2, Data S2, STAR Methods.

617

618 **Figure 3. Mechanical and cell-based 2D simulation models of ovule primordium development predict**
619 **that ovule shape depends on cell growth anisotropy.**

620 (A) Reference model for FEM-based simulation of ovule primordium growth. Growth stability is reached
621 at T=24. The fine lines indicate principal strain directions (white: expansive strain, red: compressive
622 strain).
623 (B) FEM-based simulation omitting the anisotropic growth parameter (FEM-model 3) showing abnormal
624 ovule dome shape at T=24.
625 (C) Reference model for Mass Spring (MS) cell-based simulation of ovule primordium growth. Growth
626 stability is reached at T=190.
627 (D) MS cell-based simulation with isotropic cell growth (MS-model 3), showing enlarged apex and dome
628 shape and abnormal cell division planes in L1, at T=190.
629 (E) Reference model for MS cell-based simulation showing emergence of L2 cell anisotropy at T=58.
630 (F) MS cell-based simulation MS-Model 3 (see Table 2) showing reduced L2 cells anisotropy at T=58.
631 Heatmaps: strain levels (A-B), growth signal intensity (C-D), 2D anisotropy index (E-F). See also Figure S3,
632 Table 2 for model hypotheses and STAR Methods.
633

634 **Figure 4. *katanin* mutants show a distinct ovule primordium architecture, primarily through altered**
635 **cell division patterns.**

636 Comparison between wild-type (WT, Ws-4 accession) and *katanin (kat, bot1-7* allele*)* ovule primordia
637 unless indicated otherwise.
638 (A) 3D segmented images at stage 1-II. External organ view (top) and longitudinal sections (bottom) are
639 shown. Scale bar 10µm. See Data S2a for full datasets.
640 (B-D) Morphological difference between WT and *kat* primordia measured by their volume (B), the aspect
641 ratio (C), and aspect ratio to bounding box occupancy relationship (D). D, Left: scheme representing the
642 bounding box capturing the primordium's 3D surface. See also Figure S4A.
643 (E) Quantification of cell number, cell volume, and sphericity in comparisons of L1 *versus* L2,L3 and
644 apical *versus* basal domains at stage 0-III. See also Figure S4C.

645 (F) Mitotic activity domains are altered in *kat* primordia. Top: Heatmap of Log2 fold change of mitotic
646 activity in the *kat* mutant (*lue1* allele) *versus* WT (Col-0) *per* domain, at two developmental stages. The
647 frequency of mitoses was measured as in Figure 2. Full maps of mitotic activity in different mutant
648 alleles are shown Figure S4E. Bottom: representative images of *kat* primordia (*lue1* allele) expressing
649 *pCYCB1.1::db-GFP*. Dashed lines mark L2 apical cells. Magenta signal: Renaissance SR2200 cell wall label.
650 Scale bar 10µm.
651 (G) Mean cell volume and sphericity are increased in *katanin* L2 apical cells in contact with the SMC.
652 SMC, cells in contact with the SMC, and cells not in direct contact with the SMC, are compared at stage
653 0-III.
654 Color code in all plots: Dark red: WT; Salmon: *kat* mutant. Error bars: standard error of the mean. Differences
655 between WT and *kat* mutants in (B), (C), (E), and (G) were assessed using a Mann Whitney U test; a two-
656 tailed Fischer's exact test was used in (F). P values: *p≤0.05, **p≤0.01, ***p≤0.001. See also Figure S4 and
657 Data S4.
658
659 **Figure 5. Altered ovule primordium architecture in *katanin* mutants is associated with multiple SMCs.**

660 (A) SMCs lose their typical pear shape in *katanin* mutants. 3D images of the apical-most cells according
661 to top and side views as indicated, showing the SMC (yellow), SMC neighbors (purple), and the L1 dome
662 (transparent red).
663 (B) Differential properties of L2,L3 apical domain cells (SMC and SMC neighbors) in terms of cell number,
664 mean cell volume, ellipticity, and sphericity at stage 1-II. See also Figure S5A and Data S4b.
665 (C) Representative images of cleared wild-type (WT) and *kat* ovule primordia. The percentage indicate
666 the frequency of ovules showing one SMC for WT primordia, or multiple SMC candidates (dashed lines)
667 for *kat* primordia.
668 (D-E) Representative images and quantification of SMC fate markers in WT and *kat* primordia: eviction of
669 the *H1.1::H1.1-GFP* marker (green, D) and ectopic expression of *KNU::nls-YFP* (yellow, E) in more than
670 one cell *per* primordia, are increased in *kat* primordia. See also Figure S5B.
671 (F) The meiotic marker *AtDMC1::GUS* is ectopically expressed in *kat* ovules.
672 Mutant alleles: *bot1-7* (A-B), *mad5* (C-E), *lue1* (F). Additional *kat* alleles, stages and detailed quantifications
673 are presented Figure S5 and Data S5. Magenta signal in (B) and (C): Renaissance SR2200 cell wall label. Scale
674 bars for (C), (D) and (E): 10µm. n: number of ovules scored. Error bar: standard error of the mean. Differences
675 between WT and *kat* genotypes were assessed using a Mann Whitney U test in (B), and a two-tailed Fischer's
676 exact test in (D), (E), and (F). P values: *p≤0.05, **p≤0.01, ***p≤0.001. See also Figure S5 and Data S5.
677
678 **Figure 6. The formation of a single SMC stems from a canalization process.**

679 (A-B) In wild-type (WT) plants, ovule primordia harbour one (Class A) or occasionally two (Class B) SMC
680 candidates with the frequency of class B gradually decreasing during development, reminiscent of
681 developmental canalization. Typical images obtained by tissue clearing with SMC candidates highlighted
682 in yellow (A) and plots showing the percentages of classes A and B (B). The frequency of class B ovules is
683 significantly reduced from stage 1-I, suggesting that canalization (represented by the red dashed line)
684 occur before that stage. The plot coloration is a visual aid only.

685 (C) Developmental canalization is delayed in *katanin* mutants (*kat*, *mad5* allele). The proportion of class
686 B ovules is significantly reduced from stage 2-II only. Quantifications for two additional mutants carrying
687 *kat* alleles are presented Figure S6A. The plot coloration is a visual aid only.
688 (D) The candidate SMCs initially identified as enlarged cells consistently show an enlarged nucleus in
689 both class A and class B primordia. Nuclear area is compared between the candidate SMCs (cSMC) and
690 surrounding L2 and L1 cells (see Figure S6D and STAR Methods for further details). Box plots include
691 jittered data points to visualize data variability. Red lines represent the median of cSMC nuclear area for
692 comparison with other cell types. Equivalent quantifications for stage 0-III are presented in Figure S6E.
693 (E-F) During Phase I (stages 0-II, 0-III), S-phase is detected in candidate SMCs at higher frequency than in
694 neighbors cells in class A ovules, and in both SMC candidates in class B ovules. Representative images of
695 ovule primordia showing the speckled S-phase pattern of the *pPCNA1::PCNA:sGFP* reporter (green) (E).
696 Magenta signal: Renaissance SR2200 cell wall label. Scale bar 10µm. Quantification of speckled S-phase
697 pattern in the SMC candidate and L2 neighbors (class A ovules) or in both SMC candidates (class B) (F).
698 (G-H) During Phase II (stages 1-I to 2-II), in class A wild-type ovule primordia, SMC exits S-phase, and
699 neighbors cells re-enter S-phase; while *katanin* primordia show the opposite pattern.. Representative
700 images of class A ovule primordia primarily showing the nucleoplasmic G1/G2-phase pattern of
701 *pPCNA1::PCNA:sGFP* in SMCs at stages 1-II (left panel) and 2-II (middle panel); and of the speckled S-
702 phase pattern in neighbors cells (right panel). Quantification of speckled S-phase pattern in SMC
703 candidates and neighbors in Phase II wild-type and *katanin* primordia (I). Representative images and
704 quantifications of Phase I *katanin* primordia and of class B primodia are presented in Figure S6F-H. See
705 also Figure 2H.
706 (I) Model for the role of *KATANIN* in primordium growth and SMC differentiation (graphical abstract). In
707 WT primordia, SMC differentiation follows a developmental canalization process influenced by cell
708 growth anisotropy that shapes the primordium apex. In *kat* mutants, reduced anisotropy modifies the
709 cell proliferation pattern, enlarges the apex and the L2,L3 apical domain, leading to multiple SMC
710 candidates (delayed canalization). We propose that ovule primordium shape, controlled by anisotropic
711 cell growth, determines SMC singleness.
712 *Images*: scale bars : 10um. *Graphs*: n= total number of ovules. Error bar: standard error of the mean (F, I).
713 Differences between cell types, domains, or genotypes as indicated in the graphs were assessed using
714 *Wilcoxon signed rank test in (D), and* a two-tailed Fischer's exact test in B, C, F, and I. P values: *p≤0.05,
715 **p≤0.01, ***p≤0.001. Quantifications for additional alleles and detailed quantifications are provided in
716 Figure S6 and Data S6.
717
718 **Supplementary Figures Legends**
719
720 **Figure S1_Related to Figure 1. Approaches for morphodynamic analyses of ovule primordium**
721 **development using a reference set of 3D segmented images.**

722 (A) OvuleViz, an interactive interface enabling the analysis of segmented data based on exported cell
723 statistics. The different snapshots display several features of OvuleViz, enabling the generation of plots
724 from chosen cell statistics for chosen ovule primordium stage, genotype, cell labels or groups thereof
725 (viewpoints).

726 (B) Examples of plot types that can be generated by OvuleViz.
727 (C) Possibility to export all or a subset of data as summary table or raw dataframe for further analyses
728 external to OvuleViz.
729 (D) PCA of cell descriptors from the wild-type reference dataset (*Arabidopsis* Col-0) (see DataS1), for all
730 cell types and all stages. PCA was performed on a dataset containing Sphericity, Ellipticity oblate,
731 Ellipticity prolate, Area, and Volume. Only the first and the second Principal Components (PCs) are
732 shown. The loading plot and table indicate the variables' contribution to each component.
733 (E) Same as (D) for all cell types grouped by stage: stage 0 (0-I; 0-II), stage 1 (1-I; 1-II), and stage 2 (2-I; 2-
734 II). Variables' contributions are presented by loading plots for each PC and summary table.
735
736 **Figure S2_Related to Figure 2. Ovule primordium morphogenesis involves domain-specific cell division**
737 **and anisotropic cell growth patterns.**

738 (A) Average cell number and cell volume in wild-type ovule *Col-0* primordium during development.
739 Mann Whitney U test was used to assess the difference of each stage relative to the previous stage.
740 Related to Figure 2A.

741 (B) Extraction of overall ovule height and width used in Figure 2B,C. (a) segmented stack imported in
742 MorphoGraphX [31], (b) continuous surface mesh created in MoprhoGraphX with the minimal curvature
743 projected, the clipping plane is shown (dashed grid), (c) comparison between cell-mesh and continuous
744 mesh, (d) Longitudinal section of the mesh showing maximal (1) and minimal (2 and 3) curvature points.
745 Heatmap: minimal curvature mm^{-1}. Related to Figure 2B-C.
746 (C) Box plots and line plot (error bar is standard error of the mean) showing the mean cell volume in
747 each ovule domain during all developmental time points. Mann Whitney U test was used to assess the
748 difference between stages (L1 apical). Related to Figure 2I.
749 (D) Scatter plots comparing the cell volume of SMC (yellow) to the average cell volume of other cells
750 types (same color code as in Figure 1) *per* ovule primordium, per stage. Related to Figure 2I.
751 (E) Comparison of cell volume between L1 and L2L3 cells in Phase I ovule primordia (stages 0-I to 0-III).
752 Wilcoxon Signed Rank test was used to assess the difference between domains. Related to Figure 2J.
753 (F) Quantification of cell sphericity and ellipticity (prolate and oblate, see STAR methods) at all ovule
754 primordium domains during development.
755 (G) Computation of covariance matrix eigenvalues for cell anisotropy analysis: Left: semi-automated cell
756 type classification showing labelled cells along a longitudinal cut of an ovule. L2 SMC neighbors (orange)
757 stands for all L2 cells sharing a portion of their wall with the SMC (yellow). Unlabelled cells (in red) are
758 not considered in the analysis. For the inner cells, the main anisotropy axis (the eigenvector of the
759 covariance matrix corresponding to the biggest eigenvalue) is shown with a white line. Right:
760 representation of eigenvectors of the covariance matrix (white lines) used for the PCA analysis on cell
761 anisotropy on a random cell. The eigenvectors are scaled by their own eigenvalue normalized over the
762 sum of the three eigenvalues. The longest eigenvector is aligned with the longest cell axis, the shortest
763 with the shortest cell axis and the mid eigenvector with the cell axis orthogonal to the other two (and of
764 intermediate length). Related to Figure 2K.

765 (H) SMC anisotropy index calculated from Maximum (dark blue), Mid (mid blue) and Minimum (pale blue)
766 eigenvalues, normalized by the sum of all, from stage 0-I to stage 2-I. Related to Figure 2K. P values: *p≤0.05,
767 **p≤0.01, ***p≤0.001. See also DataS2.
768
769 **Figure S3_Related to Figure 3. FEM- and MS-based simulations, reference models, and additional**
770 **variations.**
771 (A) *Time series of the FEM reference simulation: FEM-Model 1 and its preparation.* **Left***:* reference
772 simulation progression; the lines represent the in-plane principal strains: white for extensive, red for
773 compressive. The heatmap represents the trace of the Green-Lagrange strain tensor. **Right**: preparation
774 of the reference template (a-c) and initial parameters (d). (a-c) the starting template is a flat tissue
775 representation distinguishing L1 and inner layers on which anisotropic material (a, Young's modulus E2),
776 material stiffness (b, Young's modulus E1E3), and the growth signal (c, Kpar) domain are set. The white
777 lines indicate the direction of fiber reinforcement for the anisotropic material (a), the intensity of the
778 stiffness in the isotropic component of the material (b), the direction of signal-based growth, which is
779 orthogonal to the fiber reinforcement direction (c). In addition, all lateral boundaries of the simulation
780 template (except the top one) were fixed in all degrees of freedom. The table (d) integrates the visual
781 information with global parameters. See additional explanations in the STAR Methods.
782 (B) *Variation of the signal-based growth distribution with respect to the FEM- and MS-based reference*
783 *models.* For all model variations, the result is shown for the continuous FEM-based simulations (top) and
784 the MS-based simulations (bottom) at the simulation time point indicated (T). (**a**) Model 4: the signal is
785 allowed to diffuse broadly. In both FEM- and MS-based simulations, the primordium is broader and the
786 flanks are not orthogonal to the surface (arrow) as in the reference models. (**b**) Models 5: L1-driven
787 growth hypothesis (1). Here the growth-specifying signal is set at a high and fixed (i.e., non-diffusing)
788 concentration only in the L1. In both simulations, these conditions allow the formation of a protrusion
789 but not a realistic primordium. For both simulations, the growth time went beyond the reference time
790 to reach the same final height as in the reference models and to compensate for the prescribed reduced
791 growth intensity. Specific observations are made for the different simulations: FEM-Model 5 shows high
792 compression forces below the L1 (arrow: compressive areas are marked by the blue color and red lines).
793 One interpretation is that these compressions may arise because the L1 "collapses" towards the center
794 in the absence of inner tissue growth. Note the narrower apical, subepidermal domain than in the
795 reference model. Furthermore, in the periclinal direction the L1 experiences significant compressions
796 (indicated by the red lines). MS-Model 5: the growth is not balanced and generated an unstable apex
797 (arrow, winding in different directions during growth, see Movie S2). (**c**) Models 6: L1-driven growth
798 hypothesis (2). Here the growth signal is restricted solely to the L1. In this case, the difference is striking
799 for both FEM- and MS-based simulations: the models are not able to create a significant buckle and,
800 even if strain-based growth is permitted, the inner tissue is not pulled upwards. The growing part of the
801 L1 ends being compressed by the non-growing counterpart (as shown by the compressive strain marked
802 in blue in the image for the FEM-based simulation), causing the simulation to numerically fail earlier
803 than the reference (FEM) or in any case not forming a primordium (MS). (**d**) Models 7: exclusive inner-
804 tissue growth hypothesis. Here, the growth signal is absent in the L1. The L1 performs exclusively
805 passive strain-based relaxation. In this model, we test whether it is plausible that growth can be entirely
806 initiated by the inner tissues, provided the L1 has a higher ability to relax (compared to the remaining

807 tissue) due to induced strain. In such a scenario, the inner layer, which is prescribed to grow as in the
808 reference model, pushes the L1, causing accumulation of tensile strains in the periclinal direction that
809 get released due to passive strain-based relaxation. Both FEM- and MS-based simulations are able to
810 produce a digit-shaped protrusion, even if, in the FEM-based simulation, it is shorter with less straight
811 flanks (i.e., smoother transition from the placenta to the flanks; dotted arrow). This can be explained by
812 the absence of compressive strains at the base of the ovule (plain arrow) in comparison with the
813 reference model. The MS-based model displays a primordium with increased width at the apex. A
814 possible explanation for this may be the absence of growth constraints generated by the L1. In both
815 cases, the passive strain-based relaxation coefficient of the L1 was higher than in the reference model.
816 Whether this is biologically relevant remains to be addressed experimentally.
817 (C) *Models varying passive strain-based relaxation and material properties.* Results are shown for the
818 continuous FEM-based simulations (top) and the MS-based simulations (bottom) at the simulation time
819 point indicated (T). (**a**) Models 8: absence of passive strain-based relaxation in all the tissue. In both
820 simulations, this results in a poorly developed primordium (and numerically the simulation fail earlier
821 than the reference time), likely due to the accumulation of high strains (and stresses), particularly visible
822 in the FEM-based model (high accumulation of compressive and tensile strains near each other in the
823 inner tissue as well as in the L1, arrows). (**b**) Model 8a: variation of the previous model with absence of
824 passive strain-based relaxation only in the L1. In both simulations, the primordium is shorter than in the
825 reference case, although less severe in the FEM-based simulation. Specifically, in the L1 there is a high
826 accumulation of tensile stresses on the outer walls in the apical portion and in the inner walls at the
827 base (arrows). (**c**) FEM-Model 2: absence of anisotropic material properties in all tissues. Although the
828 simulation produced a well-shaped primordium, the L1 is slightly thicker (double sided arrow, 1.2-fold
829 compared to reference Model 1) and there is a larger L2,L3 apical domain characterized by a principal
830 strain oriented 90° to that in the reference model (insets). These morphological differences with the
831 reference model can be explained by the fact that passive strain-based relaxation in an isotropic
832 material has an equal effect in the periclinal and the anticlinal direction, producing a thicker L1 and a
833 rounder dome. In (**d**) FEM-based Model 2b: variation of previous Model 2. Here, only the L1 has
834 anisotropic material properties. This restores the L1 thickness control but the abnormally high intensity
835 and modified direction of compressive strains are similar to that in Model 2.
836 (D) *Mass spring reference model and initial template preparation, comparison with data from real*
837 *ovules.* Top left: MS-Model 2 simulation at four different time points. The heatmap indicates the
838 intensity of the growth-specifying signal. Bottom left: reference simulation performed on a template
839 obtained from a real ovule placenta (see also STAR Methods). Top right: Initial parameters at simulation
840 start. Field values as indicated (**a-g**) used to set up the reference configuration shown on the placenta at
841 simulation time 0 and MS global parameters (**h**). More details can be found in the STAR
842 Methods. Bottom right: comparison between simulation and real primordia. *Image*: 3D, segmented
843 ovule primordia stage 0-II from the wild-type reference set (see main text), longitudinal view: the SMC
844 (orange) is outlined in a white triangular mesh (color-code refers to cell volume). Its morphology is to be
845 compared to SMC candidates produced in the reference Model MS-Model 2 (e.g., T=134 for grid-based
846 simulation and T=108 for real-image template-based simulation): the cell is elongated, centrally located
847 in the apical dome and presents a broader upper periclinal wall surface compared to the bottom one.
848 *Plot*: comparison of height-width ratio along simulation progression in MS-Model 2 and developmental

849 progression in real (from segmented images of the wild-type reference set, see main text). For the
850 simulation, two equi-distanced time-points between the 1st (T = 0) and the last simulation time step (T =
851 190) have been used to compute the values for intermediate phases.
852 (E) *Model intervening on SMC division*. In the reference MS-Model 2, there is no explicit rule preventing
853 division of the SMC candidate. To analyze the consequence of SMC growth on primordium growth in our
854 models, we prevented the SMC candidate to divide at simulation time T = 110. Under the reference
855 conditions where the turgor pressure is the same among all subepidermal cells, this generates a gigantic
856 cell exerting a considerable tensile stretch on the surrounding cells, deforming the whole domain. This
857 suggests that, in reality, SMC growth might be compensated by a reduction in turgor pressure, a
858 hypothesis that needs to be tested. Note that the two direct adjacent cells have an elongated shape
859 reminiscent of companion cells.
860
861 **Figure S4_Related to Figure 4. *katanin* ovule growth defects.**
862
863 (A) *Ovule size, aspect ratio, bounding box, and bounding box occupancy.* Ovule volume was calculated as
864 the sum of cell volumes for individual ovules (OvuleViz data). For each ovule, the volume of their fitting
865 bounding box (represented Figure 4D) was calculated using box side lengths given in Imaris (Bitplane) on
866 ovule primordia treated as Surface objects (see STAR methods). Bounding box occupancy was calculated
867 as the ratio of the ovule volume relative to its bounding box volume. The aspect ratio was calculated as
868 the height (C length of the bounding box) divided by the mean of the width and depth lengths (A and B
869 lengths of the bounding box). Man Whitney U test was used to assess differences between genotypes.
870 Related to Figure 4B-D.
871 (B) Comparison of cell number, cell volume, and sphericity in WT (Ws-4) and *kat (bot1-7)* ovule
872 primordia. Man Whitney U test was used to assess the differences between genotypes.
873 (C) Global PCA analyses of cell's characteristics in *kat versus* WT ovules (Ws-4). PCA was performed on a
874 dataset containing Sphericity, Ellipticity oblate, Ellipticity prolate, Area, and Volume measurements of
875 WT and *kat* cells from ovules at the indicated stages (0-III, 1-I, 1-II). Cell types are labelled according to
876 colour code indicated. 95% confidence ellipses are indicated (dashed lines). Only the first and the
877 second Principal Components (PCs) are shown. The loading plots indicate the contributions of the
878 variables to each component. Related to Figure 4E.
879 (D) Comparison of mean cell number and volume in apical versus basal domains, and in L1 versus L2,L3
880 layers between WT (Ws-4) and *kat* (*bot1-7*) ovule primordia. Man Whitney U test was used to assess
881 differences between genotypes. Related to Figure 4E.
882 (D) Comparison of cell sphericity as in (C). Related to Figure 4E.
883 (E) Mitotic activity in distinct domains of the ovule primordium of WT (Col, Ws.4) and *kat* (*lue1, bot1-7*)
884 mutant plants. WT data are presented also in Figure 2 and shown here for better comparison only. The
885 frequency of mitoses was scored using the *pCYCB1.1::db-GFP* reporter. Dark gray regions mark Phase I
886 developmental stages. Two-tailed Fischer's exact test was used to assess differences between domains
887 in the genotypes. Significant P values (*p≤0.05, **p≤0.01, ***p≤0.001) are indicated for the different
888 domains in coloured boxes below the heatmaps. See also Data S2 and DataS4. Related to Figure 4F.
889

890 **Figure S5_Related to Figure 5. Altered ovule primordium architecture in *katanin* mutants is associated**
891 **with multiple SMCs.**
892
893 (A) Comparison of volume and sphericity of L2,L3 apical domain cells in wild-type (WT, Ws-4) and
894 *katanin* (*kat*, *bot1-7* allele). Mann Whitney U test was used to assess the differences between genotypes
895 for the mean cell volume and sphericity visualized by boxplots. Related to Figure 5B.
896 (B) Representative images and quantification of WT (WS-4) and *kat* (*bot1-7*) ovule primordia expressing
897 *pKNU::nls-YFP* (yellow signal), specifically expressed in the SMC. *kat* ovules show ectopic subepidermal
898 cells with YFP signal, confirming SMC fate acquisition. Related to Figure 5E.
899 (C) Representative images (10µm maximum intensity projections of image stacks) and quantification of
900 WT (WS-4) and *kat* (*bot1-7*) ovule primordia expressing the *pWOX2:CenH3-GFP* marker (green signal),
901 labeling centromeres from the functional megaspore (FM) stage onward. Cells ectopically expressing the
902 marker are detected in *kat* at both early (before centromeres condensation – left panel) and late (after
903 centromeres condensation – right panel) stages of FM formation. Note that ectopic FMs are aligned with
904 the normal, most basal (chalazal) FM, suggesting that they belong to the same tetrad. They also display
905 a similar number of centromeres (5) visible on the projections. Quantification was performed on pooled
906 early and late FM stages. Related to Figure 5D-F.
907 White signal: Renaissance SR2200 cell wall label. Scale bar: 10µm. n: number of ovules scored. Error
908 bar: standard error of the mean. Two-tailed Fischer's exact test was used to assess differences between
909 domains in the distinct genotypes. P values: *p≤0.05, **p≤0.01, ***p≤0.001. See also Data S5.
910
911 **Figure S6_ Related to Figure 6. The formation of a single SMC emerges from a canalization process**
912 **controlled by *KATANIN*.**

913 (A) Canalization of SMC fate in different *katanin* alleles (*kat*; *lue1, bot1-7*) and respective wild-type
914 backgrounds (WT; Col, Ws-4). Percentages of class A and B primordia based on cleared tissue
915 preparations as shown Figure 6A. The proportion of primordia with several SMC candidates at stage 0-II
916 gradually decreases with developmental progression while the proportion of ovules with a single SMC
917 increases, suggesting canalization. A significant delay in canalization (dashed red line) in *kat* mutants
918 was confirmed by a two-tailed Fischer's exact test (see also DataS2). Related to Figure 6B-C.

919 (B-C) Ectopic expression of SMC fate in *kat* primordia (*mad5* allele) compared to wild-type (WT; Col).
920 Percentage of ovule primordia showing *H1.1-GFP* marker [54] eviction (B); and *KNU-nlsYFP* marker [55]
921 expression (C) in more than one SMC candidate at all developmental stages. Two-tailed Fischer's exact
922 test was used to assess differences between genotypes. Related to Figure 6B-C and Figure 6D-E.
923 (D-E) Nuclear area as a marker of SMC candidates. Illustration of the cells selected for nuclear area
924 measurements in representative class A and B ovules (D). We measured nuclei in two L1 cells types (L1a,
925 apical position and L1b, closer to the placenta), cSMC: candidate SMC; L2b: a neighbouring L2 cell.
926 Dashed circles mark the nuclei of these cells used in the measurements. Related to Figure 6D.
927 Quantification of nuclear area as shown in (D) for class A and B in WT and *kat* (*mad5* allele) ovule
928 primordia at stage 0-III (E). Box plot representations include jittered points to visualize data variability.
929 Red lines represent the median of cSMC nuclear area for comparison with the other cells. Wilcoxon

930 signed rank test was used to assess difference between SMC and the other cell types. Related to Figure
931 6D.
932 (F-H) Frequency of SMC showing an S-phase pattern in *kat* primordia. Representative images (F); green,
933 *pPCNA1::PCNA:sGFP*, magenta: Renaissance SR2200 cell wall label. Scale bar 10µm. Related to Figure 6F,
934 6H. Quantification of S-phase occurrence within the L2 apical domain cells of class A and class B *katanin*
935 (*mad5*) ovule primordia in Phase I (stages 0-II to 0-III) (G). Quantification of S-phase occurrence at the
936 cells of the L2 apical domain of class B WT and *kat* (*mad5 allele*) ovule primordia in Phase II (stages 1-I to
937 2-II) (H). The plotted frequencies refer to the number of primordia showing a speckled
938 *pPCNA1::PCNA:sGFP* pattern in SMC candidates. Two-tailed Fischer's exact test was used to assess
939 differences between genotypes. Related to Figure 6H.
940 All graphs: n= number of ovules scored. Error bar: standard error of the mean. P values: *p≤0.05,
941 **p≤0.01, ***p≤0.001. See also Data S6.

942

943

944 **References**

945

946 1. Extavour, C.G., and Akam, M. (2003). Mechanisms of germ cell specification across the
947 metazoans: epigenesis and preformation. Development *130*, 5869-5884.
948 2. Kimble, J. (2011). Molecular regulation of the mitosis/meiosis decision in multicellular
949 organisms. Cold Spring Harb Perspect Biol *3*, a002683.
950 3. Bowman, J.L.e. ed. (1993). Arabidopsis : an Atlas of Morphology and Development. (Berlin &
951 New York: Springer-Verlag).
952 4. Schneitz, K., Hülskamp, M., and Pruitt, R.E. (1995). Wild-type ovule development in Arabidopsis
953 thaliana: a light microscope study of cleared whole-mount tissue. Plant Journal *7*, 731-749.
954 5. Bajon, C.H., C.; Motomayor, J.C.; Sauvanet, A.; Robert D. (1999). Megasporogenesis in
955 Arabidopsis thaliana L.: an ultrastructural study. Sexual Plant Reproduction *12*, 99-109.
956 6. Schmidt, A., Schmid, M.W., and Grossniklaus, U. (2015). Plant germline formation: common
957 concepts and developmental flexibility in sexual and asexual reproduction. Development *142*,
958 229-241.
959 7. Rodriguez-Leal, D., Leon-Martinez, G., Abad-Vivero, U., and Vielle-Calzada, J.P. (2015). Natural
960 variation in epigenetic pathways affects the specification of female gamete precursors in
961 Arabidopsis. Plant Cell *27*, 1034-1045.
962 8. Sheridan, W.F., Avalkina, N.A., Shamrov, II, Batygina, T.B., and Golubovskaya, I.N. (1996). The
963 mac1 gene: controlling the commitment to the meiotic pathway in maize. Genetics *142*, 1009-
964 1020.
965 9. Sheridan, W.F., Golubeva, E.A., Abrhamova, L.I., and Golubovskaya, I.N. (1999). The mac1
966 mutation alters the developmental fate of the hypodermal cells and their cellular progeny in
967 the maize anther. Genetics *153*, 933-941.
968 10. Nonomura, K., Miyoshi, K., Eiguchi, M., Suzuki, T., Miyao, A., Hirochika, H., and Kurata, N.
969 (2003). The MSP1 gene is necessary to restrict the number of cells entering into male and
970 female sporogenesis and to initiate anther wall formation in rice. Plant Cell *15*, 1728-1739.
971 11. Zhao, X., de Palma, J., Oane, R., Gamuyao, R., Luo, M., Chaudhury, A., Herve, P., Xue, Q., and
972 Bennett, J. (2008). OsTDL1A binds to the LRR domain of rice receptor kinase MSP1, and is
973 required to limit sporocyte numbers. Plant J *54*, 375-387.

12. Garcia-Aguilar, M., Michaud, C., Leblanc, O., and Grimanelli, D. (2010). Inactivation of a DNA methylation pathway in maize reproductive organs results in apomixis-like phenotypes. Plant Cell *22*, 3249-3267.
13. Olmedo-Monfil, V., Duran-Figueroa, N., Arteaga-Vazquez, M., Demesa-Arevalo, E., Autran, D., Grimanelli, D., Slotkin, R.K., Martienssen, R.A., and Vielle-Calzada, J.P. (2010). Control of female gamete formation by a small RNA pathway in Arabidopsis. Nature *464*, 628-632.
14. Schmidt, A., Wuest, S.E., Vijverberg, K., Baroux, C., Kleen, D., and Grossniklaus, U. (2011). Transcriptome analysis of the Arabidopsis megaspore mother cell uncovers the importance of RNA helicases for plant germline development. PLoS Biol *9*, e1001155.
15. Su, Z., Zhao, L., Zhao, Y., Li, S., Won, S., Cai, H., Wang, L., Li, Z., Chen, P., Qin, Y., et al. (2017). The THO Complex Non-Cell-Autonomously Represses Female Germline Specification through the TAS3-ARF3 Module. Curr Biol *27*, 1597-1609 e1592.
16. Su, Z., Wang, N., Hou, Z., Li, B., Li, D., Liu, Y., Cai, H., Qin, Y., and Chen, X. (2020). Regulation of Female Germline Specification via Small RNA Mobility in Arabidopsis. Plant Cell.
17. Zhao, X., Bramsiepe, J., Van Durme, M., Komaki, S., Prusicki, M.A., Maruyama, D., Forner, J., Medzihradszky, A., Wijnker, E., Harashima, H., et al. (2017). RETINOBLASTOMA RELATED1 mediates germline entry in Arabidopsis. Science *356*.
18. Cao, L., Wang, S., Venglat, P., Zhao, L., Cheng, Y., Ye, S., Qin, Y., Datla, R., Zhou, Y., and Wang, H. (2018). Arabidopsis ICK/KRP cyclin-dependent kinase inhibitors function to ensure the formation of one megaspore mother cell and one functional megaspore per ovule. PLoS Genet *14*, e1007230.
19. Pinto, S.C., Mendes, M.A., Coimbra, S., and Tucker, M.R. (2019). Revisiting the Female Germline and Its Expanding Toolbox. Trends Plant Sci *24*, 455-467.
20. Lora, J., Yang, X., and Tucker, M.R. (2019). Establishing a framework for female germline initiation in the plant ovule. J Exp Bot *70*, 2937-2949.
21. Waddington, C.H. (1942). Canalization of development and the inheritance of acquired characters. Nature, 563-565.
22. Scharloo (1991). Canalization: Genetic and Developmental Aspects. Annual Review of Ecology and Systematics *22*, 65-93.
23. Hallgrimsson, B., Green, R.M., Katz, D.C., Fish, J.L., Bernier, F.P., Roseman, C.C., Young, N.M., Cheverud, J.M., and Marcucio, R.S. (2019). The developmental-genetics of canalization. Semin Cell Dev Biol *88*, 67-79.
24. Grossniklaus, U., and Schneitz, K. (1998). The molecular and genetic basis of ovule and megagametophyte development. Semin Cell Dev Biol *9*, 227-238.
25. Lora, J., Herrero, M., Tucker, M.R., and Hormaza, J.I. (2017). The transition from somatic to germline identity shows conserved and specialized features during angiosperm evolution. New Phytol *216*, 495-509.
26. Luptovciak, I., Komis, G., Takac, T., Ovecka, M., and Samaj, J. (2017). Katanin: A Sword Cutting Microtubules for Cellular, Developmental, and Physiological Purposes. Front Plant Sci *8*, 1982.
27. Ovecka, M., Luptovciak, I., Komis, G., Samajova, O., Samakovli, D., and Samaj, J. (2020). Spatiotemporal Pattern of Ectopic Cell Divisions Contribute to Mis-Shaped Phenotype of Primary and Lateral Roots of katanin1 Mutant. Front Plant Sci *11*, 734.
28. Truernit, E., Bauby, H., Dubreucq, B., Grandjean, O., Runions, J., Barthelemy, J., and Palauqui, J.C. (2008). High-resolution whole-mount imaging of three-dimensional tissue organization and gene expression enables the study of Phloem development and structure in Arabidopsis. Plant Cell *20*, 1494-1503.
29. Mendocilla-Sato, E.B., C. (2017). Analysis of 3D Cellular Organization of Fixed Plant Tissues Using a User-guided Platform for Image Segmentation. Bio-protocols *7*, e2355.

1022 30. Ubeda-Tomas, S., Federici, F., Casimiro, I., Beemster, G.T., Bhalerao, R., Swarup, R., Doerner,
1023 P., Haseloff, J., and Bennett, M.J. (2009). Gibberellin signaling in the endodermis controls
1024 Arabidopsis root meristem size. Curr Biol *19*, 1194-1199.
1025 31. Barbier de Reuille, P., Routier-Kierzkowska, A.L., Kierzkowski, D., Bassel, G.W., Schupbach, T.,
1026 Tauriello, G., Bajpai, N., Strauss, S., Weber, A., Kiss, A., et al. (2015). MorphoGraphX: A
1027 platform for quantifying morphogenesis in 4D. Elife *4*, 05864.
1028 32. Bassel, G.W., Stamm, P., Mosca, G., Barbier de Reuille, P., Gibbs, D.J., Winter, R., Janka, A.,
1029 Holdsworth, M.J., and Smith, R.S. (2014). Mechanical constraints imposed by 3D cellular
1030 geometry and arrangement modulate growth patterns in the Arabidopsis embryo. Proc Natl
1031 Acad Sci U S A *111*, 8685-8690.
1032 33. Echevin, E., Le Gloanec, C., Skowronska, N., Routier-Kierzkowska, A.L., Burian, A., and
1033 Kierzkowski, D. (2019). Growth and biomechanics of shoot organs. J Exp Bot *70*, 3573-3585.
1034 34. Coen, E., Rolland-Lagan, A.G., Matthews, M., Bangham, J.A., and Prusinkiewicz, P. (2004). The
1035 genetics of geometry. Proc Natl Acad Sci U S A *101*, 4728-4735.
1036 35. Kennaway, R., Coen, E., Green, A., and Bangham, A. (2011). Generation of diverse biological
1037 forms through combinatorial interactions between tissue polarity and growth. PLoS Comput
1038 Biol *7*, e1002071.
1039 36. Boudon, F., Chopard, J., Ali, O., Gilles, B., Hamant, O., Boudaoud, A., Traas, J., and Godin, C.
1040 (2015). A computational framework for 3D mechanical modeling of plant morphogenesis with
1041 cellular resolution. PLoS Comput Biol *11*, e1003950.
1042 37. Rodriguez, E.K., Hoger, A., and McCulloch, A.D. (1994). Stress-dependent finite growth in soft
1043 elastic tissues. J Biomech *27*, 455-467.
1044 38. Kuchen, E.E., Fox, S., de Reuille, P.B., Kennaway, R., Bensmihen, S., Avondo, J., Calder, G.M.,
1045 Southam, P., Robinson, S., Bangham, A., et al. (2012). Generation of leaf shape through early
1046 patterns of growth and tissue polarity. Science *335*, 1092-1096.
1047 39. Bozorg, B., Krupinski, P., and Jonsson, H. (2016). A continuous growth model for plant tissue.
1048 Phys Biol *13*, 065002.
1049 40. Mosca, G.A., M.; Strauss, S.; Runions, R.; Sapala, A.; Smith, R.S. (2018). Modeling plant tissue
1050 growth and cell division. In Mathematical Modelling in Plant Biology. (Springer, Cham), pp.
1051 107-138.
1052 41. Smith, R.S. (2009). Modeling plant morphogenesis and growth. . In New Trends in the Physics
1053 andMechanics of Biological Systems. Lecture Notes of the Les Houches Summer School.,
1054 Volume 22, M.G. Ben Amar, A.; Müller, M.M.; Cugliandolo, L., ed. (Oxford: Oxford University
1055 Press).
1056 42. Amar, M.B.G., A.; Müller, M.M.; Cugliandolo, L. (2011). New Trends in the Physics and
1057 Mechanics of Biological Systems, Volume 92, (Oxford: Oxford University Press).
1058 43. Bichet, A., Desnos, T., Turner, S., Grandjean, O., and Hofte, H. (2001). BOTERO1 is required for
1059 normal orientation of cortical microtubules and anisotropic cell expansion in Arabidopsis. Plant
1060 J *25*, 137-148.
1061 44. Burk, D.H., and Ye, Z.H. (2002). Alteration of oriented deposition of cellulose microfibrils by
1062 mutation of a katanin-like microtubule-severing protein. Plant Cell *14*, 2145-2160.
1063 45. Bouquin, T., Mattsson, O., Naested, H., Foster, R., and Mundy, J. (2003). The Arabidopsis lue1
1064 mutant defines a katanin p60 ortholog involved in hormonal control of microtubule orientation
1065 during cell growth. J Cell Sci *116*, 791-801.
1066 46. Brodersen, P., Sakvarelidze-Achard, L., Bruun-Rasmussen, M., Dunoyer, P., Yamamoto, Y.Y.,
1067 Sieburth, L., and Voinnet, O. (2008). Widespread translational inhibition by plant miRNAs and
1068 siRNAs. Science *320*, 1185-1190.

1069 47. Uyttewaal, M., Burian, A., Alim, K., Landrein, B., Borowska-Wykret, D., Dedieu, A., Peaucelle,
1070 A., Ludynia, M., Traas, J., Boudaoud, A., et al. (2012). Mechanical stress acts via katanin to
1071 amplify differences in growth rate between adjacent cells in Arabidopsis. Cell *149*, 439-451.
1072 48. Hervieux, N., Dumond, M., Sapala, A., Routier-Kierzkowska, A.L., Kierzkowski, D., Roeder, A.H.,
1073 Smith, R.S., Boudaoud, A., and Hamant, O. (2016). A Mechanical Feedback Restricts Sepal
1074 Growth and Shape in Arabidopsis. Curr Biol.
1075 49. Ren, H., Dang, X., Cai, X., Yu, P., Li, Y., Zhang, S., Liu, M., Chen, B., and Lin, D. (2017). Spatio-
1076 temporal orientation of microtubules controls conical cell shape in Arabidopsis thaliana petals.
1077 PLoS Genet *13*, e1006851.
1078 50. Wightman, R., Chomicki, G., Kumar, M., Carr, P., and Turner, S.R. (2013). SPIRAL2 determines
1079 plant microtubule organization by modulating microtubule severing. Curr Biol *23*, 1902-1907.
1080 51. Zhang, Q., Fishel, E., Bertroche, T., and Dixit, R. (2013). Microtubule severing at crossover sites
1081 by katanin generates ordered cortical microtubule arrays in Arabidopsis. Curr Biol *23*, 2191-
1082 2195.
1083 52. Luptovciak, I., Samakovli, D., Komis, G., and Samaj, J. (2017). KATANIN 1 Is Essential for
1084 Embryogenesis and Seed Formation in Arabidopsis. Front Plant Sci *8*, 728.
1085 53. Komis, G., Luptovciak, I., Ovecka, M., Samakovli, D., Samajova, O., and Samaj, J. (2017). Katanin
1086 Effects on Dynamics of Cortical Microtubules and Mitotic Arrays in Arabidopsis thaliana
1087 Revealed by Advanced Live-Cell Imaging. Front Plant Sci *8*, 866.
1088 54. She, W., Grimanelli, D., Rutowicz, K., Whitehead, M.W., Puzio, M., Kotlinski, M., Jerzmanowski,
1089 A., and Baroux, C. (2013). Chromatin reprogramming during the somatic-to-reproductive cell
1090 fate transition in plants. Development *140*, 4008-4019.
1091 55. Tucker, M.R., Okada, T., Hu, Y., Scholefield, A., Taylor, J.M., and Koltunow, A.M. (2012).
1092 Somatic small RNA pathways promote the mitotic events of megagametogenesis during female
1093 reproductive development in Arabidopsis. Development *139*, 1399-1404.
1094 56. Agashe, B., Prasad, C.K., and Siddiqi, I. (2002). Identification and analysis of DYAD: a gene
1095 required for meiotic chromosome organisation and female meiotic progression in Arabidopsis.
1096 Development *129*, 3935-3943.
1097 57. Klimyuk, V.I., and Jones, J.D. (1997). AtDMC1, the Arabidopsis homologue of the yeast DMC1
1098 gene: characterization, transposon-induced allelic variation and meiosis-associated expression.
1099 Plant J *11*, 1-14.
1100 58. De Storme, N., Keceli, B.N., Zamariola, L., Angenon, G., and Geelen, D. (2016). CENH3-GFP: a
1101 visual marker for gametophytic and somatic ploidy determination in Arabidopsis thaliana. BMC
1102 Plant Biol *16*, 1.
1103 59. Yokoyama, R., Hirakawa, T., Hayashi, S., Sakamoto, T., and Matsunaga, S. (2016). Dynamics of
1104 plant DNA replication based on PCNA visualization. Sci Rep *6*, 29657.
1105 60. Strzalka, W., and Ziemienowicz, A. (2011). Proliferating cell nuclear antigen (PCNA): a key
1106 factor in DNA replication and cell cycle regulation. Ann Bot *107*, 1127-1140.
1107 61. Whitewoods, C.D., and Coen, E. (2017). Growth and Development of Three-Dimensional Plant
1108 Form. Curr Biol *27*, R910-R918.
1109 62. Wolny, A., Cerrone, L., Vijayan, A., Tofanelli, R., Barro, A.V., Louveaux, M., Wenzl, C., Strauss,
1110 S., Wilson-Sanchez, D., Lymbouridou, R., et al. (2020). Accurate and versatile 3D segmentation
1111 of plant tissues at cellular resolution. Elife *9*.
1112 63. Hartmann, J., Wong, M., Gallo, E., and Gilmour, D. (2020). An image-based data-driven analysis
1113 of cellular architecture in a developing tissue. Elife *9*.
1114 64. Reik, W., and Surani, M.A. (2015). Germline and Pluripotent Stem Cells. Cold Spring Harb
1115 Perspect Biol *7*.

1116 65. Huang, B.Q., and Russell, S.D. (1992). Female Germ Unit: Organization, Isolation, and Function.
1117 International Review of Cytology *140*, 233-293.
1118 66. Heitzler, P., and Simpson, P. (1991). The choice of cell fate in the epidermis in Drosophila. Cell
1119 *22*, 1083-1092.
1120 67. Pujadas, E., and Feinberg, A.P. (2012). Regulated noise in the epigenetic landscape of
1121 development and disease. Cell *148*, 1123-1131.
1122 68. Chan, C.J., Heisenberg, C.P., and Hiiragi, T. (2017). Coordination of Morphogenesis and Cell-
1123 Fate Specification in Development. Curr Biol *27*, R1024-R1035.
1124 69. Huang, A., Rupprecht, J.F., and Saunders, T.E. (2020). Embryonic geometry underlies
1125 phenotypic variation in decanalized conditions. Elife *9*.
1126 70. Gruel, J., Landrein, B., Tarr, P., Schuster, C., Refahi, Y., Sampathkumar, A., Hamant, O.,
1127 Meyerowitz, E.M., and Jonsson, H. (2016). An epidermis-driven mechanism positions and
1128 scales stem cell niches in plants. Sci Adv *2*, e1500989.
1129 71. Savaldi-Goldstein, S., Peto, C., and Chory, J. (2007). The epidermis both drives and restricts
1130 plant shoot growth. Nature *446*, 199-202.
1131 72. Landrein, B., Kiss, A., Sassi, M., Chauvet, A., Das, P., Cortizo, M., Laufs, P., Takeda, S., Aida, M.,
1132 Traas, J., et al. (2015). Mechanical stress contributes to the expression of the STM homeobox
1133 gene in Arabidopsis shoot meristems. Elife *4*, e07811.
1134 73. Fal, K., Asnacios, A., Chaboute, M.E., and Hamant, O. (2017). Nuclear envelope: a new frontier
1135 in plant mechanosensing? Biophys Rev *9*, 389-403.
1136 74. Peaucelle, A., Braybrook, S.A., Le Guillou, L., Bron, E., Kuhlemeier, C., and Hofte, H. (2011).
1137 Pectin-induced changes in cell wall mechanics underlie organ initiation in Arabidopsis. Curr Biol
1138 *21*, 1720-1726.
1139 75. Hervieux, N., Tsugawa, S., Fruleux, A., Dumond, M., Routier-Kierzkowska, A.L., Komatsuzaki, T.,
1140 Boudaoud, A., Larkin, J.C., Smith, R.S., Li, C.B., et al. (2017). Mechanical Shielding of Rapidly
1141 Growing Cells Buffers Growth Heterogeneity and Contributes to Organ Shape Reproducibility.
1142 Curr Biol *27*, 3468-3479 e3464.
1143 76. Long, Y., Cheddadi, I., Mosca, G., Mirabet, V., Dumond, M., Kiss, A., Traas, J., Godin, C., and
1144 Boudaoud, A. (2020). Cellular Heterogeneity in Pressure and Growth Emerges from Tissue
1145 Topology and Geometry. Curr Biol *30*, 1504-1516 e1508.
1146 77. Beauzamy, L., Nakayama, N., and Boudaoud, A. (2014). Flowers under pressure: ins and outs of
1147 turgor regulation in development. Ann Bot *114*, 1517-1533.
1148 78. Bencivenga, S., Simonini, S., Benkova, E., and Colombo, L. (2012). The transcription factors
1149 BEL1 and SPL are required for cytokinin and auxin signaling during ovule development in
1150 Arabidopsis. Plant Cell *24*, 2886-2897.

1151

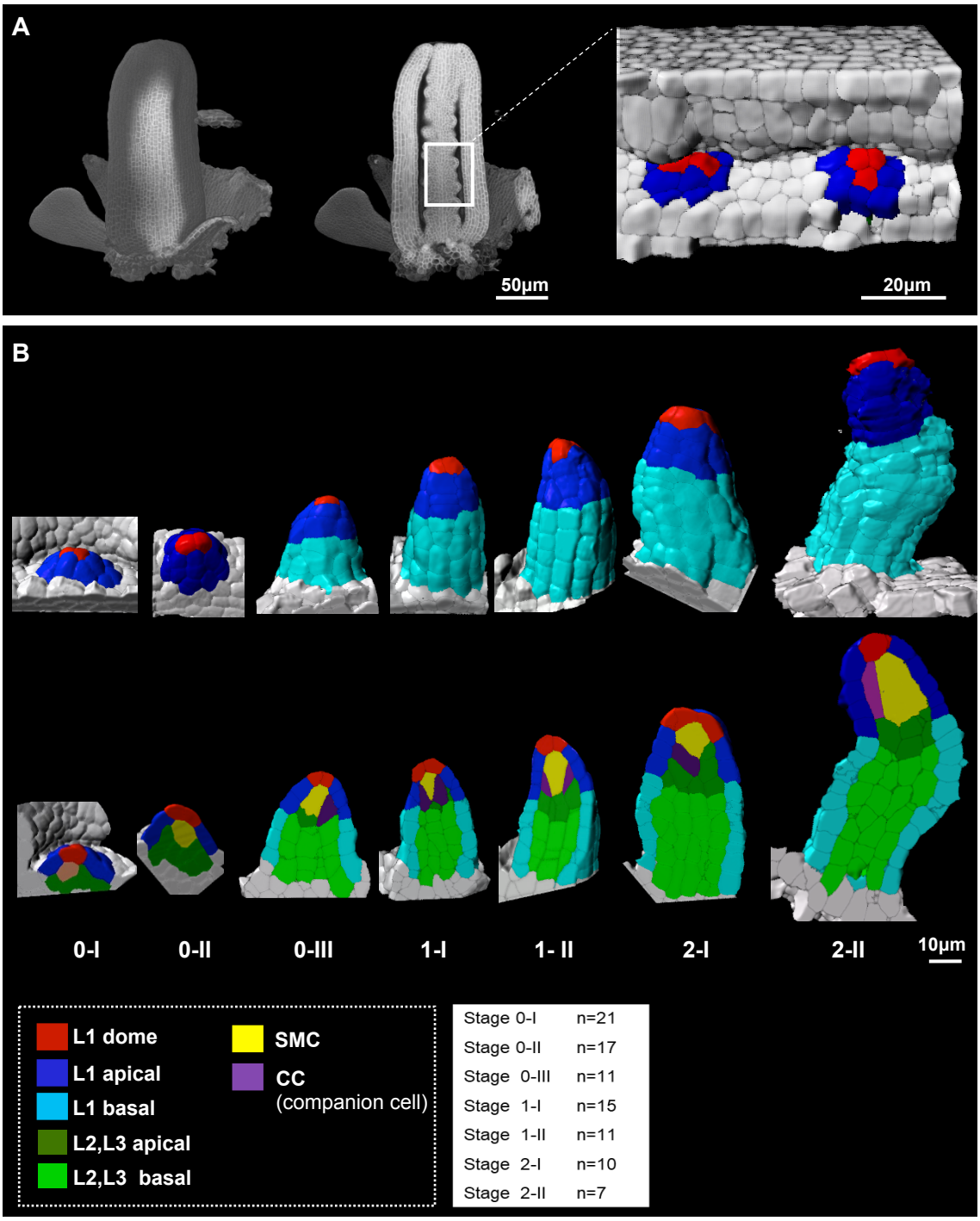

Figure 1. Reference set of 3D segmented images capturing Arabidopsis ovule primordium growth at cellular resolution.

(A) 3D reconstruction of a whole gynoecium stained with PS-PI (cell wall dye) and visualized by CSLM. The cross section allows showing the nascent ovule primordia attached to the placenta.

(B) Ovule primordium developmental stages (0-I to 2-II) and organ viewpoints (domains) defined for the 3D quantitative analysis. All segmented data can be analyzed by an interactive interface named OvuleViz. See also Figure S1A-C.

n= number of ovules analyzed. Segmented images for all developmental stages are provided in Data S1. See also STAR Methods.

	0-I			0-II			0-III		
Cells above placenta*	2.5	(±3.5)	(n=21)	3.6	(±0.5)	(n=17)	5.9	(±1.0)	(n=11)
range (min-max)	2	-	3	3	-	4	5	-	8
total # cells	28	(±5.7)	(n=21)	38	(±8.0)	(n=17)	80	(±8.4)	(n=11)
width (µm) (W)	23	(±3.5)		26.3	(±2.4)		28.0	(±3.1)	
height (µm) (H)	5.3	(±1.2)		11.9	(±2.1)		22.5	(±3.6)	
H:W ratio	0.2	(±0.04)	(n=13)	0.45	(±0.06)	(n=14)	0.8	(±0.12)	(n=8)

	1-I			1-II		
cells above placenta*	7.3	(±1.3)	(n=15)	9.7	(±1.0)	(n=11)
range (min-max)	6	-	10	8	-	11
total # cells	105	(±10.6)	(n=15)	128	(±18.0)	(n=11)
width (µm) (W)	27	(±2.0)		27.8	(±3.5)	
height (µm) (H)	30	(±2.8)		39	(±5.9)	
H:W ratio	1.1	(±0.10)	(n=6)	1.4	(±0.22)	(n=8)

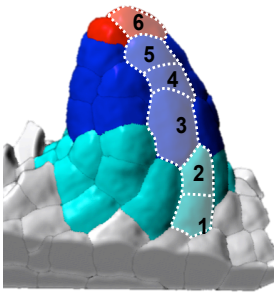

	2-I			2-II		
cells above placenta*	10	(±1.1)	(n=10)	12.6	(±1.0)	(n=7)
range (min-max)	9	-	12	11	-	14
total # cells	151	(±18.9)	(n=10)	165	(±19.8)	(n=7)

* scoring the length of L1 cell file above placenta

Table 1. Classification criteria of Arabidopsis ovule primordia

The table summarizes general characteristics of ovule primordia per stage: cell "layers" above the placenta scored as the number of L1 cells in a cell file drawn from the basis to the top, range thereof, total cell number, ovule shape including height, width, aspect ratio.

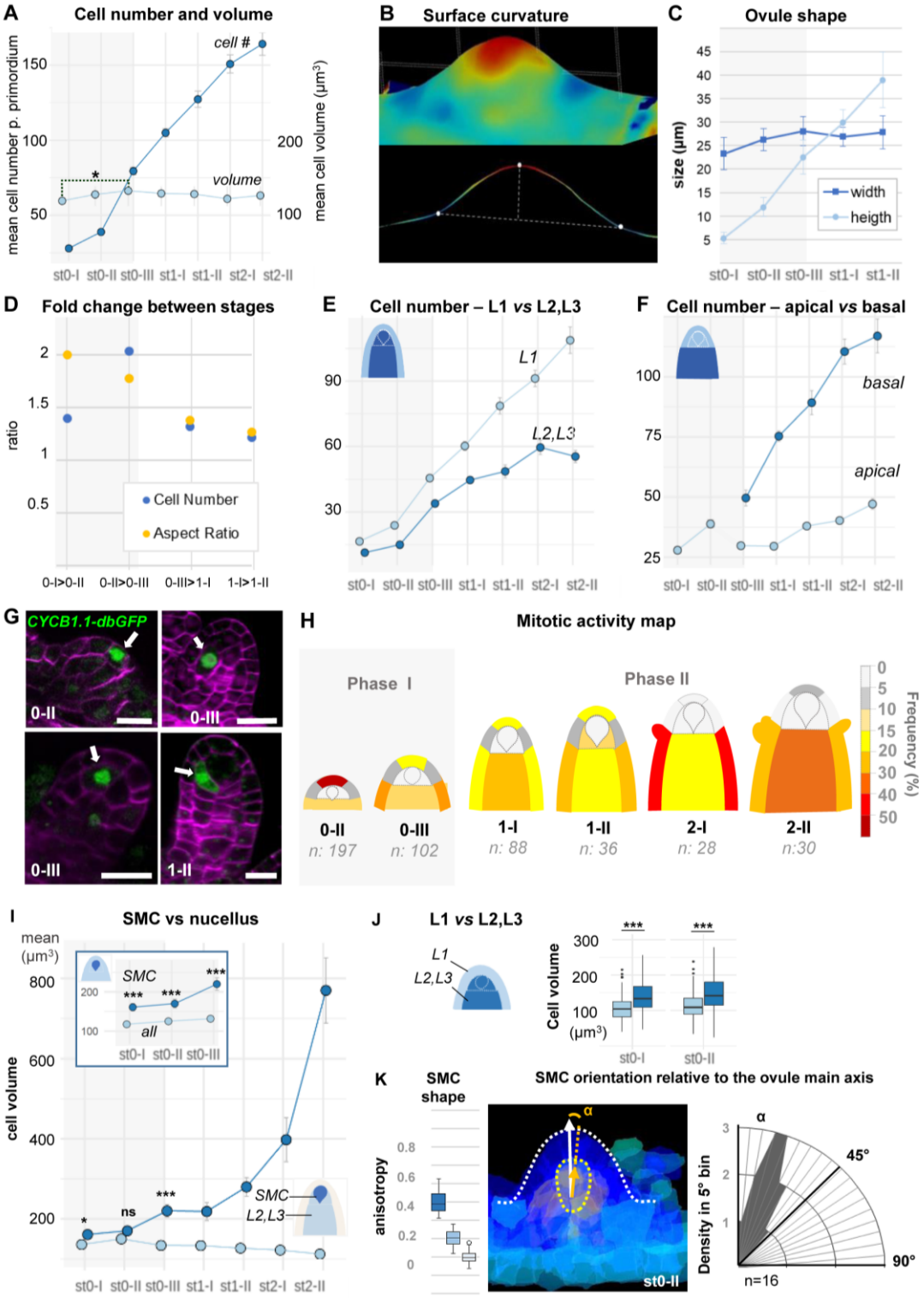

Figure 2. Ovule primordium morphogenesis involves domain-specific cell division and anisotropic cell growth patterns.

(A) Mean cell number *per* ovule increases mainly during stages 0-I to 0-III (Phase I), whereas cell volume *per* ovule remains constant on average across primordium development (stages 0-I to 2-II).
(B) Representative image of a continuous surface of an ovule primordium mesh and its projected median plane. Dashed lines indicate the minimal and maximal curvature points used to measure organ height and width. Color scale: minimal curvature mm-1 (see also Figure S2B). *Continued on next page*

Figure 2- continued

(C) Anisotropic organ growth during Phase I and until stage 1-II. Mean width and height were quantified *per* stage.

(D) Phase I captures a distinct growth dynamic compared to Phase II. Fold-change of cell number and aspect ratio between stages are plotted.

(E) Mean cell number is increased at the L1 *versus* L2,L3 layers across developmental stages.

(F) Mean cell number is increased in the basal *versus* apical domain across developmental stages.

(G) Representative images of ovule primordia expressing the M-phase reporter *pCYCB1.1::db-GFP.* White arrows indicate dividing cells. Magenta signal: Renaissance SR2200 cell-wall label. Scale bar: 10µm.

(H) Domain-specific map of mitotic activity during ovule primordium development, scored using the *pCYCB1.1::db-GFP* reporter. The frequency of mitoses was calculated *per* ovule domain at each developmental stage and color-coded as indicated in the bar (right). n: total number of scored ovules.

(I) Mean SMC volume (dark blue) is significantly increased as compared to L2,L3 cells (pale blue) from stage 0-III onward, on even at earlier stages as compared to all other cells (inset).

(J) Mean cell volume is increased in L2,L3 cells as compared to L1 cells, at the two early developmental stages (st0-I, st0-II).

(K) The SMC consistently displays anisotropic shape with main axis of elongation aligned with ovule growth axis. The SMC anisotropy index (boxplot, left; stage 0-II, n=16 ovules) was calculated from the Maximum (dark blue), Minimum (light blue) and Medium (medium blue) covariance matrix eigenvalues, computed from 3D segmented cells (see Figure S2G). Image (middle): illustration of the SMC main anisotropy axis (orange arrow) related by an angle 'alpha' to the main axis of the ovule primordium (white arrow), stage 0-II. Radar plot (right): 'alpha' angle measured on z projections for n=16 ovule primordia at stage 0-II. See also Star Methods.

Error bars: Standard errors to the mean. Differences between cell types or primordium domains were assessed using a two-tailed Man Whitney U test in (A) and (I); a two-tailed Wilcoxon signed rank test in (J). *p≤0.05, **p≤0.01, ***p≤0.001. See also Figure S2, Data S2, STAR Methods.

Modeling hypotheses		Models							
		1	2	3	4	5	6	7	8
Growth anisotropy		●	●	-	●	●	●	●	●
Material anisotropy		●	-	○	○	○	○	○	○
Passive Strain-based relaxation		●	●	●	●	●	●	●	-
Signal-based growth									
Distribution	L1 only	-	-	-	-	-	●	-	-
	Inner tissue only (pit-shape)	-	-	-	-	-	-	●	-
	L1 + inner tissue (pit-shape)	●	●	●	-	●	-	-	●
	L1 + inner tissue (broad distribution)	-	-	-	●	-	-	-	-
Fixed high concentration	L1 only	-	-	-	-	●	●	-	-
	Inner tissue only	-	-	-	-	-	-	●	-
	L1 + inner tissue	●	●	●	●	-	-	-	●

Table 2. Hypotheses used to generate the mass-spring (MS) and continuous Finite Element Method (FEM) based simulations

Several growth and mechanical hypotheses were listed at start of modelling. To evaluate their effect on primordium growth each hypothesis was excluded (-) in at least one scenario. The FEM and mass-spring (MS) models presented in Figure 3 and S3 are numbered according to the scenarios (1-8) in the table. Since it is not possible for MS to simulate material anisotropy, Model 1 was only tested with FEM. Empty dots for "Material anisotropy" were considered only for the FEM models. See also STAR Methods.

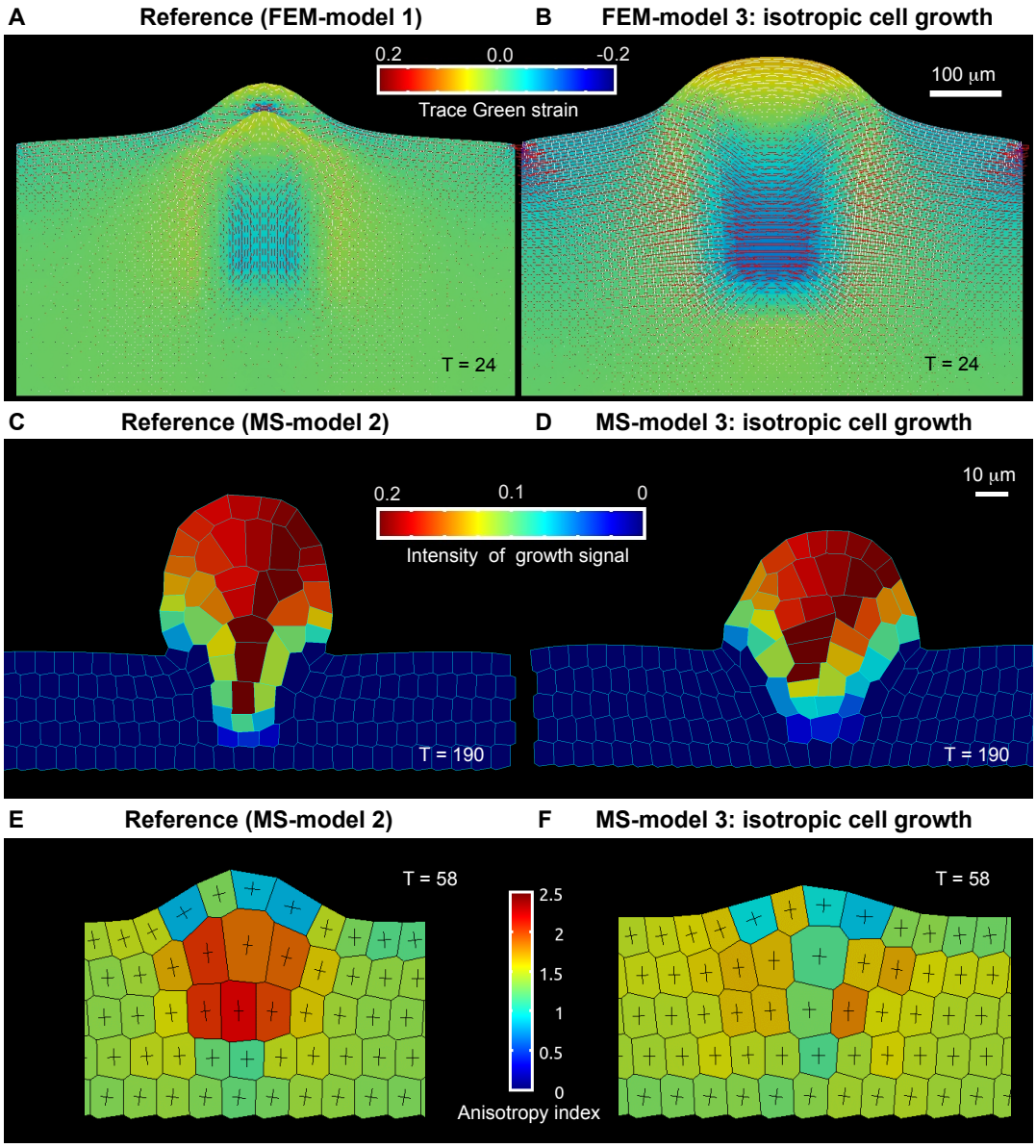

Figure 3. Mechanical and cell-based 2D simulation models of ovule primordium development predict that ovule shape depends on cell growth anisotropy.

(A) Reference model for FEM-based simulation of ovule primordium growth. Growth stability is reached at T=24. The fine lines indicate principal strain directions (white: expansive strain, red: compressive strain).

(B) FEM-based simulation omitting the anisotropic growth parameter (FEM-model 3) showing abnormal ovule dome shape at T=24.

(C) Reference model for Mass Spring (MS) cell-based simulation of ovule primordium growth. Growth stability is reached at T=190.

(D) MS cell-based simulation with isotropic cell growth (MS-model 3), showing enlarged apex and dome shape and abnormal cell division planes in L1, at T=190.

(E) Reference model for MS cell-based simulation showing emergence of L2 cell anisotropy at T=58.

(F) MS cell-based simulation MS-Model 3 (see Table 2) showing reduced L2 cells anisotropy at T=58.

Heatmaps: strain levels (A-B), growth signal intensity (C-D), 2D anisotropy index (E-F). See also Figure S3, Table 2 for model hypotheses and STAR Methods.

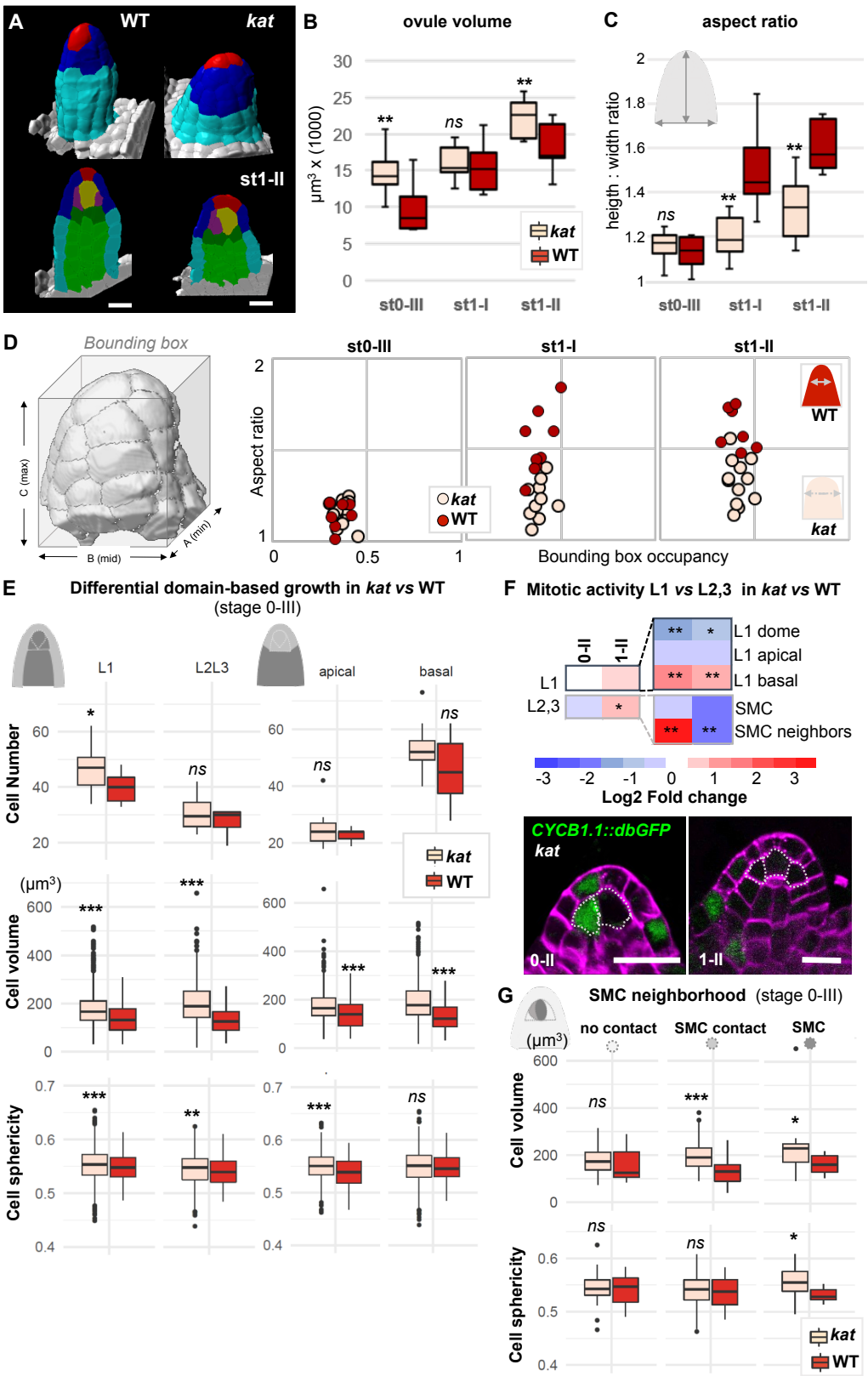

Figure 4. *katanin* mutants show a distinct ovule primordium architecture, primarily through altered cell division patterns.

Comparison between wild-type (WT, Ws-4 accession) and *katanin (kat, bot1-7* allele*)* ovule primordia unless indicated otherwise.

(A) 3D segmented images at stage 1-II. External organ view (top) and longitudinal sections (bottom) are shown. Scale bar 10µm. See Data S2a for full datasets. *Continued on next page.*

Figure 4 - Continued.

(B-D) Morphological difference between WT and *kat* primordia measured by their volume (B), the aspect ratio (C), and aspect ratio to bounding box occupancy relationship (D). D, Left: scheme representing the bounding box capturing the primordium's 3D surface. See also Figure S4A.

(E) Quantification of cell number, cell volume, and sphericity in comparisons of L1 *versus* L2,L3 and apical *versus* basal domains at stage 0-III. See also Figure S4C.

(F) Mitotic activity domains are altered in *kat* primordia. Top: Heatmap of Log2 fold change of mitotic activity in the *kat* mutant (*lue1* allele) *versus* WT (Col-0) *per* domain, at two developmental stages. The frequency of mitoses was measured as in Figure 2. Full maps of mitotic activity in different mutant alleles are shown Figure S4E. Bottom: representative images of *kat* primordia (*lue1* allele) expressing *pCYCB1.1::db-GFP*. Dashed lines mark L2 apical cells. Magenta signal: Renaissance SR2200 cell wall label. Scale bar 10µm.

(G) Mean cell volume and sphericity are increased in *katanin* L2 apical cells in contact with the SMC. SMC, cells in contact with the SMC, and cells not in direct contact with the SMC, are compared at stage 0-III.

Color code in all plots: Dark red: WT; Salmon: *kat* mutant. Error bars: standard error of the mean. Differences between WT and *kat* mutants in (B), (C), (E), and (G) were assessed using a Mann Whitney U test; a two-tailed Fischer's exact test was used in (F). P values: *$p \leq 0.05$, **$p \leq 0.01$, ***$p \leq 0.001$. See also Figure S4 and Data S4.

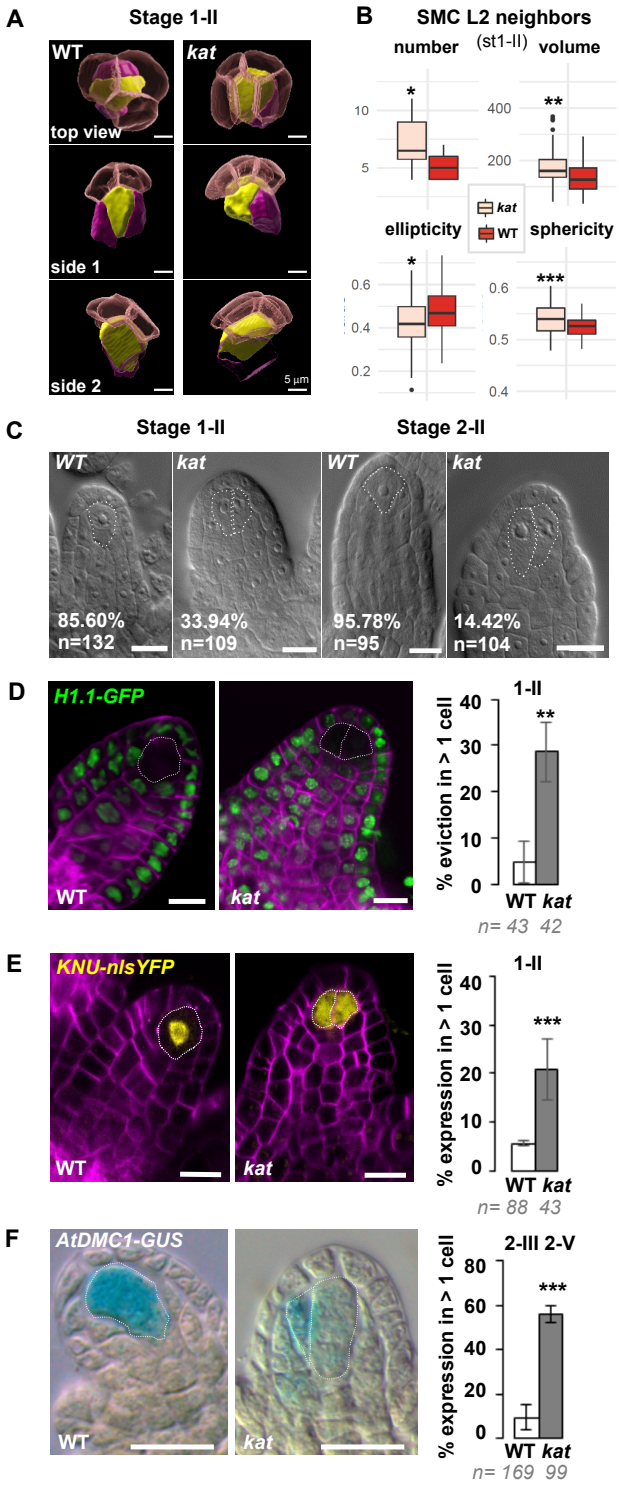

Figure 5. Altered ovule primordium architecture in *katanin* mutants is associated with multiple SMCs.

(A) SMCs lose their typical pear shape in *katanin* (*kat*) mutants. 3D images of the apical-most cells according to top and side views as indicated, showing the SMC (yellow), SMC neighbors (purple), and the L1 dome (transparent red).
(B) Differential properties of L2,L3 apical domain cells (SMC and SMC neighbors) in terms of cell number, mean cell volume, ellipticity, and sphericity at stage 1-II. See also Figure S5A and Data S4b.
(C) Representative images of cleared wild-type (WT) and *kat* ovule primordia. The % indicate the frequency of ovules showing one SMC for WT primordia, or multiple SMC candidates (dashed lines) for *kat* primordia.
(D-E) Representative images and quantification of SMC fate markers in WT and *kat* primordia: eviction of the *H1.1::H1.1-GFP* marker (green, D) and ectopic expression of *KNU::nls-YFP* (yellow, E) in more than one cell *per* primordia, are increased in *kat* primordia. See also Figure S5B.
(F) The meiotic marker *AtDMC1::GUS* is ectopically expressed in *kat* ovules.

Mutant alleles: *bot1-7* (A-B), *mad5* (C-E), *lue1* (F). Additional *kat* alleles, stages and detailed quantifications are presented Figure S5 and Data S5. Magenta signal in (B) and (C): Renaissance SR2200 cell wall label. Scale bars for (A): 5 µm ; for (C), (D), (E), (F): 10µm. n: number of ovules scored. Error bar: standard error of the mean. Differences between WT and *kat* genotypes were assessed using a Mann Whitney U test in (B), and a two-tailed Fischer's exact test in (C), (D), (E), and (F). P values: *p≤0.05, **p≤0.01, ***p≤0.001. See also Figure S5 and Data S5.

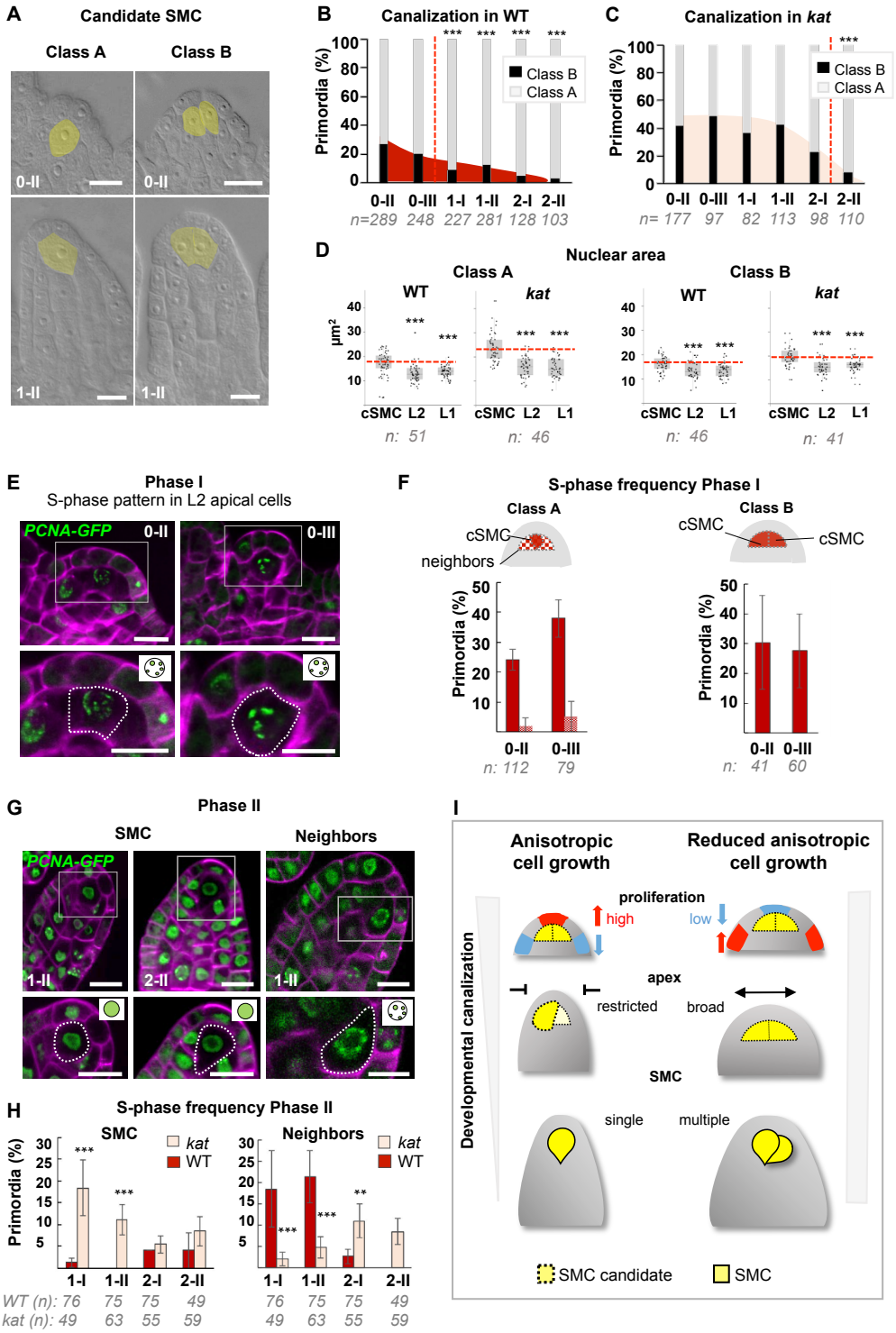

Figure 6. The formation of a single SMC stems from a canalization process.

(A-B) In wild-type (WT) plants, ovule primordia harbour one (Class A) or occasionally two (Class B) SMC candidates with the frequency of class B gradually decreasing during development, reminiscent of developmental canalization. Typical images obtained by tissue clearing with SMC candidates highlighted in yellow (A) and plots showing the percentages of classes A and B (B). The frequency of class B ovules is significantly reduced from stage 1-I, suggesting that canalization (represented by the red dashed line) occur before that stage. The plot coloration is a visual aid only.

Continued on next page

Figure 6 - continued

(C) Developmental canalization is delayed in *katanin* mutants (*kat*, *mad5* allele). The proportion of class B ovules is significantly reduced from stage 2-II only. Quantifications for two additional mutants carrying *kat* alleles are presented Figure S6A. The plot coloration is a visual aid only.

(D) The candidate SMCs initially identified as enlarged cells consistently show an enlarged nucleus in both class A and class B primordia. Nuclear area is compared between the candidate SMCs (cSMC) and surrounding L2 and L1 cells (see Figure S6D and STAR Methods for further details). Box plots include jittered data points to visualize data variability. Red lines represent the median of cSMC nuclear area for comparison with other cell types. Equivalent quantifications for stage 0-III are presented in Figure S6E.

(E-F) During Phase I (stages 0-II, 0-III), S-phase is detected in candidate SMCs at higher frequency than in neighbors cells in class A ovules, and in both SMC candidates in class B ovules. Representative images of ovule primordia showing the speckled S-phase pattern of the *pPCNA1::PCNA:sGFP* reporter (green) (E). Magenta signal: Renaissance SR2200 cell wall label. Scale bar 10µm. Quantification of speckled S-phase pattern in the SMC candidate and L2 neighbors (class A ovules) or in both SMC candidates (class B) (F).

(G-H) During Phase II (stages 1-I to 2-II), in class A wild-type ovule primordia, SMC exits S-phase, and neighbors cells re-enter S-phase; while *katanin* primordia show the opposite pattern.. Representative images of class A ovule primordia primarily showing the nucleoplasmic G1/G2-phase pattern of *pPCNA1::PCNA:sGFP* in SMCs at stages 1-II (left panel) and 2-II (middle panel); and of the speckled S-phase pattern in neighbors cells (right panel). Quantification of speckled S-phase pattern in SMC candidates and neighbors in Phase II wild-type and *katanin* primordia (I). Representative images and quantifications of Phase I *katanin* primordia and of class B primodia are presented in Figure S6F-H. See also Figure 2H.

(I) Model for the role of *KATANIN* in primordium growth and SMC differentiation (graphical abstract). In WT primordia, SMC differentiation follows a developmental canalization process influenced by cell growth anisotropy that shapes the primordium apex. In *kat* mutants, reduced anisotropy modifies the cell proliferation pattern, enlarges the apex and the L2,L3 apical domain, leading to multiple SMC candidates (delayed canalization). We propose that ovule primordium shape, controlled by anisotropic cell growth, determines SMC singleness.

Images: scale bars: 10um. *Graphs*: n= total number of ovules. Error bars: standard error of the mean (F, I). Differences between cell types, domains, or genotypes as indicated in the graphs were assessed using Wilcoxon signed rank test in (D), and a two-tailed Fischer's exact test in B, C, F, and I. P values: *p≤0.05, **p≤0.01, ***p≤0.001. Quantifications for additional alleles and detailed quantifications are provided in Figure S6 and Data S6.